Faculty of Natural Science and Technology
Department of Physics

NTNU
Innovation and Creativity

MASTER'S THESIS FOR

STUD. TECHN. ANDRÉ KAPELRUD

Thesis started:	19. januar 2009
Thesis submitted:	15. juni 2009

DISCIPLINE: CONDENSED MATTER PHYSICS

Norsk tittel:	*"Et Tunnelmikroskop for Punktkontaktundersøkelser av Magnetodynamikk i FeMn/FeNi Bilagstrukturer*
English title:	*"A Scanning Tunneling Microscope for Point Contact Investigations of Magnetodynamics in FeMn/FeNi Bilayers"*

Trondheim, 15. juni 2009

Erik Wahlström

Responsible supervisor

Associate Professor at Department of Physics

A Scanning Tunneling Microscope for Point Contact Investigations of Magnetodynamics in FeMn/FeNi Bilayers

André Kapelrud

Department of Physics — NTNU 2009

Abstract

This thesis presents the development of a scanning tunneling microscope purpose built for point contact investigations of magnetodynamics. The contributed changes include new measurement electronics, with 40-60% improvement in noise characteristics over previous versions, as well as major changes to the microscope's control software, increasing stability and functionality. The microscope is demonstrated with repeated measurements of giant magnetoresistance in a FeMn/FeNi/Cu/FeNi spin valve. These measurements are shown to induce a training effect of the exchange bias in the top FeMn/FeNi bilayer, and a logarithmic time dependence of the recovery of the exchange field is uncovered, resulting in a recovery time in the order of 50 s. Both effects are shown to be in agreement with past experimental results.

Sammendrag

Denne avhandlingen presenterer utviklingen av et tunnelmikroskop bygd med det formål å gjøre punktkontaktbaserte undersøkelser av magnetodynamikk. De bidratte endringene inkluderer ny måleelektronikk, med 40-60% forbedring i støykarakteristikk sammenlignet med tidligere versjoner, sammen med større endringer i mikroskopets programvare som bidrar til å øke mikroskopets stabilitet og funksjonalitet. Mikroskopet demonstreres ved gjentatte målinger av gigantisk magnetresistans i en FeMn/FeNi/Cu/FeNi-spinnventil. Disse vises å indusere en treningseffekt i utvekslingsfeltet til det øverste FeMn/FeNi-bilaget. Videre avdekkes en logaritmisk tidsavhengigheten i rekonvalesenseffekten til utvekslingsfeltet, som resulterer i en rekonvalesenstid på ca. 50 s. De oppnådde resultatene vises å være i overensstemmelse med tidligere eksperimentelle resultater.

Preface

This thesis marks the end of five years of studying physics here at NTNU. I started out in 2004 with the determination to study mathematics, which, even to my own surprise, I chose not to. When I was given the choice between technical physics and industrial mathematics in the third grade, I could not say no to the challenge of getting to understand physics. In retrospect, I have no reason to regret this choice, as physics has become more and more interresting for each semester here at NTNU. It has been a privilege to be able to learn from, what must be, some of the brightest minds in Norway. I hope that the reader can appreciate the work put into this dissertation.

Acknowledgements

I would like to give thanks to all the great people in the STM group at NTNU. Especially Erik Wahlström for supervising me[1]. Big thanks are due to Magne Saxegaard and Dezheng Yang for invaluable help at the lab and for tutoring me with regards to solid state physics and spintronics. All my fellow students deserves a thank you note[2]. I would also like to thank my family for all the support during the past five years. Special thanks goes out to my girlfriend, Inga[3].

Trondheim, June 15, 2009 André Kapelrud

[1] And for his ability to conjure the "reversed supervisor effect", making everything work at the times when it was needed the most

[2] E.M. "LaTeX" Viggen: thanks a bunch!

[3] ...having tolerated my mental absence for the last couple of weeks

Contents

Chapter 1

Introduction

Spintronics

Spintronics is a field of research dedicated to the investigation of the properties of devices and systems that take advantage of both the classical charge and the intrinsic quantum mechanical spin of transport particles, eg. electrons. As aligned particle spins is the cause of magnetism, the manipulation of the particle spins' phase coherence and charge dynamics can be used to manipulate magnetized domains, and vice versa. The prime example is the so called "spin polarization" that electrons is subjected to when a current goes through a transition metal with ferromagnetic properties. The electrons with spins pointing along the direction of the ferromagnet's magnetization will experience a different scattering at the ferromagnet's interfaces than electrons with opposite spin. The result will be a statistically preferred spin direction for the exiting current; we say that the current is spin polarized. Provided that the electron spins remain coherent when entering a different material, this spin polarization can be used for manipulation of charge transport properties, like conductivity, as well as for the manipulation of magnetic domains in the host material. Spintronics have seen applications in eg. read heads in modern magnetic storage hard drives, as well as in magnetic sensors (Maekawa [20]). Spintronics also have possible applications in solid state magnetic memory and data storage; as well as for GHz resonating transievers with potential applications in inter-chip communication.

The Scanning Tunneling Microscope

The *Scanning tunneling microscope* (STM) was invented by Binnig and Rohrer in 1981[1][9, 8, 7]. The STM allows a local probing of conducting surfaces by means of the quantum mechanical tunneling effect combined with a feedback positioning system. An STM has traditionally been used for surface imaging and tunneling spectroscopy applications, but by combining these techniques with the possibility of making local electrical point contacts to the surface, the STM can be used

[1] Binnig & Rohrer was awarded the Nobel prize in physics in 1986 for the invention

to study transport properties and phenomena of (magnetic) systems on a local scale.

Previous attempts by the STM group at NTNU at using a commercial STM system for spintronics related research was impaired by the properitary nature of these "black box" systems. The required modifications to low level features of these systems, which none had intimate knowledge with, proved cumbersome and in some cases impossible to correct. One example of the latter is that the commercial system used a magnetic retention mechanism for the STM tip, which behaved badly when subjected to externally applied magnetic fields. Because of this, it was decided to design and build a new STM. With this system, we hope to achieve:

- No magnetic coupling between the internal components of the STM and externally applied magnetic fields.
- Thermal and mechanical stability by design. A goal is to be able to make stable point contacts on the time scale of seconds up to several minutes.
- High resolution point contacts at high sample rates using quality data aquisition systems and high speed electronic controllers.
- Component modularity, meaning that components can be modified and replaced whenever this will be necessary. This will be in contrast to the "black box" commercial systems.
- Using the knowledge about the custom built system to develop new methods for spintronics measurements, as well as being able to tune the system's parameters to achieve better measurements using already available techniques.

This is a daunting task, but could, in the long, run prove to be a valuable asset to the STM group's toolbox for spintronics research.

Overview

This thesis is a treatize on the current state of development of the in-house custom built STM system, with special emphasis on the author's contribution to the project for the last five months as well as the the current measurements that have been performed with the system so far. The thesis structure is as follows:

Chapter 1 This chapter.

Chapter 2 The theoretical background for the scanning tunneling microscope and related technology is treated (Sec. 2.1), as well as a review of the theory and experimental results of relevant spintronics related phenomena (Section 2.2 through 2.5).

Chapter 3 This chapter is dedicated to the design of the STM scanner (Sec. 3.1); the measurement signal line related hardware, with some

components built by the author (Sec. 3.2); an overview of the control software, including the contributed changes, and the related hardware components (Sec. 3.3); the magnetic sample system used for testing and on which measurements have been performed on (Sec. 3.4).

Chapter 4 The measurement results and discussion.

Chapter 5 Conclusion and suggestions for future work on the system.

Chapter 2

Background

2.1 Scanning Tunneling Microscopy

The Scanning Tunneling Microscopy (STM) has been an import part of the surface scientist's arsenal since it's invention in 1981 by Binnig and Rohrer[9, 8, 7]. The STM makes it possible to create raster images of surfaces with atomic resolution, with a lateral resolution down to a few Ångström and a vertical resolution to a sub-Ångström range.

The principle behind the STM is that a localized quantum mechanical tunneling current can develop if a bias voltage is applied between a sample surface and an atomically sharp needle (*tip*), if the needle is brought close ($\sim 1 - 10$ Å), to the sample surface. An image of the sample surface can then be made if the tip is moved in a systematically and controlled manner over the sample while making sure that the tunneling current between the tip and the sample is constant.

2.1.1 Tunneling

According to quantum mechanics there is a small but finite probability for a particle to tunnel through a potential barrier. The transmission coefficent for tunneling of a free electron, with energy E, through a rectangular barrier, with width s and potential $U > E$, is treated in almost every introductory text on quantum mechanics. Using the wavematching method we get(see eg. Hemmer[17]) :

$$T \propto e^{-2\chi s} , \qquad \chi = \sqrt{\frac{2m(U-E)}{\hbar^2}} , \tag{2.1.1}$$

where χ is the particle's wave number in the forbidden barrier region, and T is the ratio of the incoming current density j_i to the tunneling current density j_t. Figure 2.1 shows an incoming wave with energy E tunneling through a barrier with height U.

Using the a semi-classical WKB[1]-approximation where $\hbar$ is treated as an expansion (smallness) parameter for a free particle wave-function, $\Psi(x) = e^{iS(x)\hbar}$,

[1] after Gregor Wentzel, Hendrik Kramers and Louis Brillouin

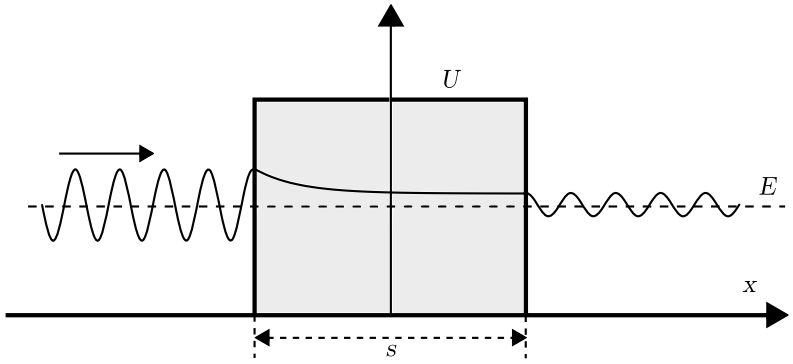

Figure 2.1: A particle coming in from the left tunnels through the classical forbidden region with width s. In the classically forbidden region, the wavefunction decays according to Eq. (2.1.1).

the probability for tunneling through a one-dimensional barrier, with a space-dependant potential $U(x)$, can be expressed, to 2^{nd} order in $\hbar$, as

$$P = \exp\left(-\frac{2}{\hbar}\int_{x_0}^{x_0+s}\chi(x)\,\mathrm{d}x\right)\ . \tag{2.1.2}$$

The transition probability from one state to another accounting for tunneling of an electron across a barrier can be evaluated to first order time independent perturbation theory

$$\omega_{fi} = \frac{2\pi}{\hbar}g_f|M_{fi}|^2, \tag{2.1.3}$$

where M_{fi} is the transition element taking the particle from an initial state Ψ_i to a final state Ψ_f (tunneling implied), and g_f is the density of final states. Bardeen [2] did such an analysis concluding that the matrix element could be expressed as

$$M_{fi} = \int_a [\Psi_i^*\hat{H}\Psi_f - \Psi_f\hat{H}\Psi_i^*]\,\mathrm{d}\tau\ , \tag{2.1.4}$$

where $\hat{H}$ is the Hamiltonian and the subscript a indicates that the volume integration is over the region where the incoming particle's wavefunction is well defined. The tunneling current density, i.e. the total tunneling probability, is then given by

$$J = e\sum_i\sum_f \omega_{fi}\ , \tag{2.1.5}$$

where e is the electron charge and the summations are over all inital states i and all final states f in the tip and sample respectivly. If a negative bias voltage is applied between the two regions and temperature effects are taken into account, then Eq. (2.1.5) will be modified by the fermi functions of the two regions. The applied bias voltage may induce a reversed current, so the total current density will be the difference between a forwards directed current and the backwards

directed current:

$$J_{\text{total}} = e \sum_{i,f} \{[1 - f(E_f + eU_B)]f(E_i) - [1 - f(E_i)]f(E_f + eU_B)\} \cdot \delta(E_i - E_f + eU_B)\omega_{fi} \ , \tag{2.1.6}$$

where $f(E)$ is the fermi function, U_B is the applied bias voltage, E_i and E_f are the initial energy levels in the tip and sample; and δ is the dirac delta function.

Eq. (2.1.6) depends on the local wave functions of both the tip and the sample surface via Eq. (2.1.4) complicating the evaluation of the tunneling current from first principles. Nevertheless, Tersoff and Hamann[32, 33] managed to alleviate this somewhat by assuming a spherical potential well for the tip. Furthermore, in the limit of small bias voltage and temperature, the tunneling current density be rewritten as

$$J \approx \sum_{i,f} \omega_{fi} \delta(E_i - E_F)\delta(E_f - E_F) \ , \tag{2.1.7}$$

where E_F is the fermi energi. They further assumed that the matrix element in ω_{fi} would be proportional to $|\Psi_f(r_0)|^2$ if the tip was localized at an arbitrary position r_0 in relation to the sample surface geometry, giving

$$J \propto \sum_{f} |\Psi_f(r_0)|^2 \delta(E_f - E_F) \ , \tag{2.1.8}$$

where the expression on the right equals the local density of states at the fermi surface as given by a point probe at the position r_0. Thus, using an ideal probe, the images produced by an STM should be contour plots of a constant part of the local density of states, where the constant level is chosen by means of keeping the tunneling current constant during scan (constant current imaging). With a more realistic probe, as the spherical approximation put forward by Tersoff and Hamann, it can be shown that the current will be given by Eq. (2.1.8) but smeared out in a "low pass" manner, blurring the actual density of states.

As can be seen from Eq. (2.1.1), and from calculations performed by Simmons in 1963[30], the tunneling probability, and hence the current density, will in the general case depend on the tip–sample separation distance in an exponential manner. If the STM tip can be brought into tunneling distance from the surface, then this exponential dependency can be utilized as an extremely sensitive distance measure. Provided that the STM's mechanical setup has enough vibration dampening, this distance measure can be used to regulate the tip's height above the sample.

2.1.2 Positioning

The initial positioning of the STM-tip from a non-contact to a tunneling contact is typically done in steps of increasing resolution. Many systems let the operator first position the tip to within a visually resolvable distance to the sample surface and then allowing finer automated computer controlled tip movement.

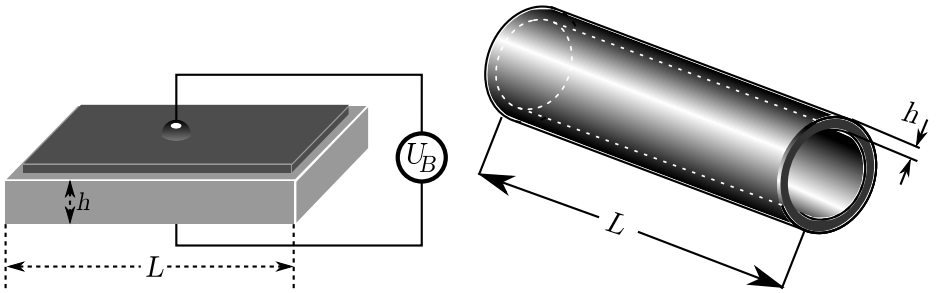

(a) (b)

Figure 2.2: a) Piezoelectric block with electrodes attached to top and bottom surface. b) Piezoelectric tube; applying a voltage between the inner and outer surface makes the crystal expand along its length L.

The coarse positioning system could be an open-loop stepper motor system, servo motor system or, because the former two have problems with mechanical vibrations, a piezoelectric crystal based drive system. In fact, as summerized by Wiesendanger [39], it was not until the piezoelectric positioning systems was adopted that the sub-nanometer resolution of the STM was achieved. Earlier tunneling based systems used servos, steppers or even manual actuation with some elaborate differential screw mechanism. The motor systems are vibrational by nature, so they inhibit the instrument from resolving corrugations at the nano- and subnanometer scale, while the manual approach just isn't viable due to irreproducibility.

Piezodrives work by applying a voltage, U, over a piezoelectric crystal which it to expand. If the crystal is cleaved to a square block with length l and thickness h, the response to voltage applied over electrodes attached across its height is given by[39]

$$\Delta l = d_{ij} \frac{l}{h} U \ , \tag{2.1.9}$$

where d_{ij} is the correct tensor element describing the crystal expansion (see Figure 2.2(a)). Alternatively, a hollow cylindrical crystal with length l and wall thickness h can be used. By applying a voltage between the inner and the outer surface, the crystal's length will change by the same amount as for the piezo block (see Figure 2.2(b)).

If two electrodes are attached on opposing sides along the outer perimeter of the hollow cylindrical crystal and a voltage is applied between the them, the crystal will bend. This bending is in the direction normal to the surface at the electrodes, and is given by

$$\Delta l_N = 2\sqrt{2} d_{ij} \frac{l^2}{2Dh} U \ , \tag{2.1.10}$$

where D is the cylinder's diameter. Alternatively, the voltage can be applied between only one of the electrodes and the inner wall, resulting in a

bend/displacement of half that of Eq. (2.1.10).

A configuration with three degrees of freedom can be made by using a tripod consisting of three piezoelements mounted along the three principal axes joined at the one end. A different approach involves using only one cylindrical crystal with multiple electrodes. By attaching four separated electrodes along the circular outer perimeter of the crystal in stead of two, the movement can be done in two lateral directions as well as along the length of the crystal. This makes for a very compact system. The one-cylinder configuration is typically used in a "fine" positioning system.

A stick slip piezodrive works by expanding or contracting the crystal slowly to one position and then quickly doing the opposite action (contraction/expansion) to accelerate the crystal. This rapid acceleration will help the crystal to overcome the static surface friction between the crystal and its' external holder resulting in that the crystal is "throwed" a tiny amount backwards or forwards.

By combining the stick-slip mechanism with the normal operation of the crystal an automated search for a tunneling current can be performed. The z-axis piezo-element is expanded in small consecutive steps while the regulation systems monitors for a tunneling current. If a current is not found within the crystal's normal physical limits, the piezoelement is contracted and then "coarse-positioned" one step closer to the sample by utilizing the stick-slip mechanism. The small-step searching is then started all over, and the whole process is repeated until a stable tunneling current is established.

For STM imaging the x- and y-axes must be able to move small consecutive steps with a resolution of about one order above the scale of the smallest surface corrugations that one wishes to resolve. The z-axis must have a resolution in the pm (10^{-12} m) scale to be able to successfully be regulated at the Ångström (1 Å $= 10^{-10}$ m) level.

The control of the voltages over the piezodrives is done in a closed loop system, using for example a regular PID (proportional+integral+derivative) controller. Usually the derivative term is left out because of it's tendency to amplify unwanted noise. The position of the z-axis can be infered from the tunneling current, allowing the tip to be brought to within a few Ångström of the sample surface. There are obviously some uncertainty in the determination of the exact distance, as the exact geometry of the tunneling junction is rarely known. The required voltages to move a certain distance laterally is calculated based on the calibrated voltage-displacement properties of the piezoelectric crystals. The control of the x- and y-axis voltages can be done in a similar manner, by measuring the voltage over one electrode in relation to the inner electrode and putting the exitation signal over the other outer electrode on the opposite side of the first one. Though, in most cases the x- and y-axes are left in an open loop without any form of feedback.

2.1.3 Tip fabrication

Since the STM technique involves moving a tip into close proximity of a sample surface, the tip is often accidentally crashed into the surface. This will dull the front of the tip degrading the STM's obtainable resolution. Consequently, the STM operator needs to be able to fabricate new tips that can be inserted into the STM.

Several different techniques for tip fabrication out of several different materials exist. Tungsten (W) tips are prepared by electrochemical etching of a thin wire. A segment of the thin ($\sim 0.1 - -1$ mm) tungsten wire is lowered a few millimeters into an alkali solution (2 M KOH). The etching of the wire will be most pronounced at the air-solution interface. As the wire is etched through the weight of the lower segment will pull on the thinnest part, eventually snapping the wire. When the wire snaps, there will be a substantial drop in the etching current. This current-drop can be used to stop the etching at the correct time. The resulting tip should be atomically sharp(see Ekvall et al. [12]).

An alternative way of fabricating tips, is by cutting a thin, ~ 0.3 mm, PtIr (we use Pt80Ir20) wire using an ordinary wire cutter. It has been shown that adequate tips will result from cutting while pulling the wire away from the wire cutter. The chance of getting a good tip with this method varies substantially, but experience shows that about one in four tries will result in a usable tip.

2.1.4 STM Measurement Types

An STM can be used for several different types of measurements. The methods include imaging of surfaces; local probing of the surface' local density of states; controlled probing; and controlled localized probing based on the recorded image.

Constant Current Imaging

As described earlier, *constant current imaging* (CCI) is the main STM imaging technique. CCI is achieved by scanning the STM in lines over the sample surface while maintaining a constant tunneling current. While the tip is scanned, the z-axis' displacement is recorded. The displacement is available as the voltage that the PID regulator has to put on the piezoelectric crystal to maintain a constant tunneling current. The resulting image can then be interpreted as a contour image of a constant level snapshot of the local density at the sample surface structure.

The alternative to CCI is scanning the tip at a constant height above the sample while monitoring the changing tunneling current. This is only applicable for relatively flat surfaces. It has the main advantage of speed, an can thus be used for recording dynamic changes in the sample's surface during eg. chemical reactions.

Tunneling spectroscopy (TS)

The tunneling spectroscopy technique consists of putting the STM tip at some selected position, lock the current to the z-axis piezodrive by means of a sample-

and-hold circuit, and then vary the bias voltage within some predefined range while sampling the tunneling current.

As found out by Bardeen in 1963[2] and Tersoff and Hamann in 1983[32] the main contribution to a tunneling current is due to the electron density of states at the surface. This was later experimentally verified by Feenstra et al. [13] who showed that the normalized differential conductance was proportional to the density of states at the surface:

$$\frac{\mathrm{d}I/\mathrm{d}U}{I/U} = \frac{\mathrm{d}\ln I}{\mathrm{d}\ln U} \propto g(eU) \ . \tag{2.1.11}$$

As such, tunneling spectroscopy is a valuable tool for investigating the surface density of states.

Point contacts

By pushing the STM tip past the "safe" zone of the tunneling domain, local contacts can be made to the sample surface. If the current through the contact and the voltage over the junction is monitored while indenting the tip, the tip can be stopped at a specified resistance. This resistance will be related to the contact area between the STM tip and the sample, making it possible to do measurements with controlled current densities running into the sample. These point contacts can also be used as a spectroscopic method for probing the dynamical properties of the structure, like electron–phonon, electron–magnon or similar interactions for energies near the fermi energy of the sample[18, 11].

If we assume that the tip has as spherical shape the contact area will have a circular shape. Electrons flowing through this orifice will be determined by the size of the constriction, described by the orifice' radius a, and by the mean free path, l, of the electrons as they move through the material.

The problem with current flowing through a small circular contact was treated classically by Maxwell already in 1904[21, 18]. His result was given by the simple expression

$$R_M = \frac{\rho}{2a} \ , \tag{2.1.12}$$

where ρ is the resistivity of the metal. This is only valid when the mean free path, l, is much smaller than the characteristic size of the constriction: $l \ll a$. However, when we have the opposite case, $l \sim a$, or more importantly when $l \gg a$; Ohm's law doesn't apply anymore as the electrons will conduct ballistically through the constriction. The conduction regime, either ballistical or diffusive, will be determined by the Knudsen ratio:

$$K = \frac{l}{a} \ . \tag{2.1.13}$$

Following Jansen et al.[18]; if the contact is a heterogeneous contact in the clean (ballistical) limit of the Knudsen number, the electrons will be propelled over the junction gaining an energy $\Delta U = eV$. Here e is the electron charge, and V is the applied junction bias voltage. From the kinetic energy $U = 1/2mv^2$, we

see that the energy increase will be given by $\Delta U = mv\Delta v = p\Delta V$. Assuming a spherical fermi surface, a resonable assumption for good metals, the electron's speed increase is given by

$$\Delta v = \frac{eV}{p_F} \ , \tag{2.1.14}$$

where p_F is the fermi momentum. This gives a current

$$I \approx An_0 e\Delta v = \frac{\pi a^2 n_0 e^2 V}{p_F} \ , \tag{2.1.15}$$

where $A = \pi a^2$ is the contact area and n_0 is the electron density at the fermi level.

The Drude resistivity is given from Newtons second law and the Lorentz force: $\Delta v \approx a\tau = \frac{eE\tau}{m}$, giving a current density at the fermi surface of: $j \approx n_0 e\Delta v = \frac{n_0 e^2 E\tau}{m}$. Assuming Ohm's law, $E \propto \sigma j$, to be in effect, the Drude resistivity for a good metal is:

$$\rho = \frac{m}{n_0 e^2 \tau} = \frac{p_F}{n_0 e^2 l} \ , \tag{2.1.16}$$

where τ is the intercollision relaxation time for the electrons at the fermi level with momentum p_F and speed $v_F = l\tau$; the last expression defining the mean free path, l, in the metal.

Inserting the Drude resistivity into Eq. (2.1.15) and integrating over all angles for the incoming electrons through the orifice, we get the Sharvin expression for ballistic currents through a circular point contact:

$$R_S = \frac{4\rho l}{3\pi a^2} \ . \tag{2.1.17}$$

For intermediate Knudsen numbers the resistance can be expressed as an interpolation between the dirty (diffusive) Maxwell resistance and the clean (ballistic) Sharvin resistance[38, 18, 11].

$$\begin{aligned} R &\approx R_S + B(K)R_M \\ R &= \frac{4\rho l}{3\pi a^2} + B(K)\frac{\rho}{2a} \ , \end{aligned} \tag{2.1.18}$$

where $B(K)$ is a slowly varying function of the Knudsen number, with $B(0) = 1$ and $\lim_{K\to\infty} B(K) = \frac{9\pi^2}{128} \approx 0.694$.

By experiment it has been established that the measured resistance through real point contacts typically has non-linear features[18, 11]. The second derivative of the voltage signal with respect to the current has been shown to have features at energies corresponding to typical phonon frequencies in the metals under investigation. Thus the voltage derivative of the combined resistance from Eq. (2.1.18), $\frac{\mathrm{d}^2 V}{\mathrm{d}^2 I} = R\frac{\mathrm{d}R}{\mathrm{d}V}$, should tell us something about the phonon density of states. It can be shown[18] that it is the derivative of the diffusive Maxwell term that will generate the features by means of an energy dependent mean free path that appears when factoring out the product ρl from both the Sharvin and the Maxwell resistance before deriving Eq. (2.1.18) with respect to the voltage.

The product ρl is considered a characteristic constant for different metals, so the factoring will introduce a single energy dependent factor $l = l(\epsilon)$ in the expression for the Maxwell resistance. The mean free path can be determined from the reciprocal sum, using Mathiesens' rule, of the scattering length of all the scatterers in the metal; including impurities, phonons and possibly also magnons. Furthermore, it can be shown that the final expression for $\frac{\mathrm{d}R}{\mathrm{d}V}$ will be proportional to the Eliasbergh function, which defines the electron-phonon interaction in a metal[18].

Point contacts can thus be used as a local spectroscopic method, useful for probing the metal structure close to the surface of the sample.

2.2 Exchange Bias

Meiklejohn and Bean reported in 1956[22] of "a new magnetic anisotropy" observed as a result of an interaction between an antiferromagnetic material and a ferromagnetic material in contact with each other. They investigated the magnetic properties of fine Co particles (~ 200 Å) with oxidied CoO shells. The cobalt particles are ferromagnetic and the cobaltous oxide are antiferromagnetic below the Néel temperature of $T_N = 293°$ K. By cooling the oxidized particles to below the Néel temperature in a saturating magnetic field, Meiklejohn and Bean observed an unidirectional exchange anistropy between the antiferromagnetic shell and the ferromagnetic particles. The exchange anisotropy introduced a shift along the field direction of the cobalt's hysteresis loop. This exchange field, H_E, can thus be described as an "exchange bias".

As summarized by Nogués and Schuller[23] the exchange anisotropy can be understood qualitively by considering the interface between an antiferromagnet and a ferromagnet aligned by an external field. The spins in the antiferromagnet are aligned along the same direction ($\pm$) as the spins in the ferromagnet. On average the interface will have a net magnetization, ie. more spins in one direction than in the other direction, thus givin a local ferromagnetic coupling to the bulk ferromagnet. The exchange interaction at the interface is therefore unidirectional. Due to the increased ferromagnetic coupling to the interface spins there will be a greater resilience against magnetization reversal due to an applied external magnetic field.

Even though the exchange bias effect has been studied heavily since it's discovery in 1956 there is a lack of good quantitative understanding of it[23, 5]. Different materials will have different surface regions, giving very different spin configuration: with possibility of both compensated and uncompensated spins on the antiferromagnetic side of the interface. This means that the picture described above does not hold in the general case. The interrested reader should see the references for a treatment of the involved physical parameters and the existing models of the phenomenon. Nevertheless, exchange bias is an important effect heavily used in both the industry and current research.

Recently, some light has been shed on the behaviour of the exchange field when the AFM/FM system is subjected to reverse magnetic fields. Xi et al. [41] concluded that the antiferromagnet relaxes towards the field direction by nucleation of the antiferromagnetic domains with orientation along the field. This effect is called the "training effect", and can be described by:

$$H_e(t) = H_E \left[2 \exp\left(-\left(\frac{t}{\tau} \right)^{\sigma} \right) - 1 \right] , \tag{2.2.1}$$

where H_E is the original exchange field, τ is a characteristic relaxation time, and $\sigma \simeq 1/3$ for many systems.

In opposition to the first exchange field reverse investigated by Xi et al., the second spontaneous reverse, ie. the recovery of the exchange bias, that happens after "training" when the external field is turned off, can be described by a logarithmic time dependence. This was seen experimentally by Pina et al. in

2004[25] and later by Dho et al. in 2006[10]. Dho et al. compared the second reverse recovery of the exchange bias to isothermal annealing of amorphous metal alloys, stating that the recovery can be regarded as a thermal activation of the AFM's local domains making it relax to a lower lying energy state.

2.3 Interlayer Exchange Coupling

Putting two macroscopic ferromagnets in close proximity to each other will result in the ferromagnets ligning up antiparallel. This effect is due to the fringing fields at the abrupt surfaces of the ferromagnets, making sure that the energy minimum is found for antiparallel alignment. For ferromagnetic layers with clean surface interfaces separated by a thin, nano meter sized, non magnetic non disturbing layer, the ferromagnetic layers should in principle be able to couple ferromagnetically if the interfaces fulfill certain properties. The coupling will be ferromagnetic (antiferromagnetic) depending on several factors like: layer separation distance, interface roughness, and the metallic properties of the layers in question.

Following the summary of Waser et al.[36], the interlayer exchange coupling can be explained by considering what happens when two 3d ferromagnetic layers, like Fe, Co or Ni, are separated by a thin paramagnetic metallic layer.

In 3d ferromagnetic metals like Fe ($3d^6 4s^2$) and Co ($3d^7 4s^2$) the density of states is asymmetric for electrons with spin parallel to the ferromagnet's magnetization (spin-up/majority electrons) in relation to electrons with spin antiparallel to the magnetization (spin-down/minority electrons). This is in contrast to metals like Cu, where the density of states around the fermi energy level is dominated by the 4s conduction band which is symmetric for both majority and minority carrier electrons. If the two types of metals are brought into contact with each other and a current is forced to run perpendicularly in relation to the surface normals, ie. a *current perpendicular to plane* (CPP) geometry; the spin-down electrons will have to be promoted from a the low 3d band in the Cu layer to the high energy 3d band in the ferromagnet, while the spin-up electrons can more easily be conducted from the 3d band in Cu to the similar 3d band in the ferromagnet. Thus, if the two magnetized layers couple ferromagnetically the minority carriers can become trapped within the paramagnetic spacer layer. The minority carriers will see a potential similar to the box potential in the separation region inversely depending on the layer thickness. If the separation layer thickness is increased, the systems energy will oscillate in a sawtooth like manner with minimums in the coupling energy given by the allowed energy levels in the spacer layer. On the other hand, if the two layers couple antiferromagnetically, the majority electrons from one layer will become minority electrons when entering the other ferromagnetic layer from the spacer layer. Thus electrons from both layers will be equally scattered at one of the paramagnet's two interfaces. This should give a constant coupling energy in the antiferromagnetic case.

Concomitantly, we would expect the coupling type between the two ferromagnetic layers to depend on the interlayer separation distance, as the system will choose between ferromagnetic or antiferromagnetic coupling based on what

minimizes the system's energy at that particular separation distance. The interlayer exchange coupling effect is therefore an important effect that can be used for both characterization and manipulation of magnetic thin film structures. In fact, it was a vital part in the research leading to the discovery of the "*giant magnetoresistance*" effect, described in the next section.

2.4 Giant Magnetoresistance

Giant magnetoresistance (GMR) is an effect observed in thin film structures containing ferromagnetic layers separated by thin paramagnetic spacer layers. Typically, a low resistance is seen when the FM layers' magnetizations have parallel alignment; and high resistance is seen when the magnetizations align antiparallely. Like the interlayer exchange coupling, the GMR effect is critically dependent on the different scattering rates experienced by spin-up (majority) and spin-down (minority) electrons crossing the interfaces between the ferromagnetic (FM) layers and non-magnetic (NM) layers. Consequently, the GMR effect is only visible in structures where the electrons' spin coherence length is smaller than the FM layers' separation distances.

A GMR structure can be modelled as a two channel–two series resistor model as proposed by Pratt et al.[26]. In this model the two channels represents the two carriers: minority and majority carriers in relation to the first ferromagnet. Each parallel channel is then composed of two resistors in series (see Figure 2.3). If the two ferromagnets' magnetizations are parallel the majority carriers will conduct with low resistance through their channel, while the minority carriers will conduct with a high resistance due to severe scattering at the ferromagnet–paramagnet interface. If the two ferromagnets' magnetizations are antiparallel both carrier types will experience scattering at one of the interfaces, giving a high resistive element in each channel. As resistors in parallel are given by the reciprocal of the sum of resiprocal resistances the total resistance will be small for the parallel case and large for the antiparallel case.

The GMR effect was first discovered by Baibich et al.[1] by sending a current through a superlattice of Fe and Cr layers. The interlayer separation distance was such that the Fe layers coupled antiferromagnetically. By applying an external magnetic field, it's magnitude depending on the coupling strength between the layers, the magnetization in the films could be brought into parallel alignment. By sending a current through the structure while ramping the external field, Baibich et al. observed a "giant", up to 50%, change in the resistance of the structure.

At the same time as Baibich et al. made their discovery, a different group (see Binasch et al.[6]) made a similar discovery in a FeCr trilayered structure showing a 1.5% change in the magnetoresistance when reaching parallel alignment of the two Fe layers. The discovery of the GMR effect was awarded the Nobel price in physics in 2007. The price was awarded to Albert Fert, the leader of the research group behind the 1988[1] discovery; and to Peter Grünberg, the leader of the second group mentioned above[6].

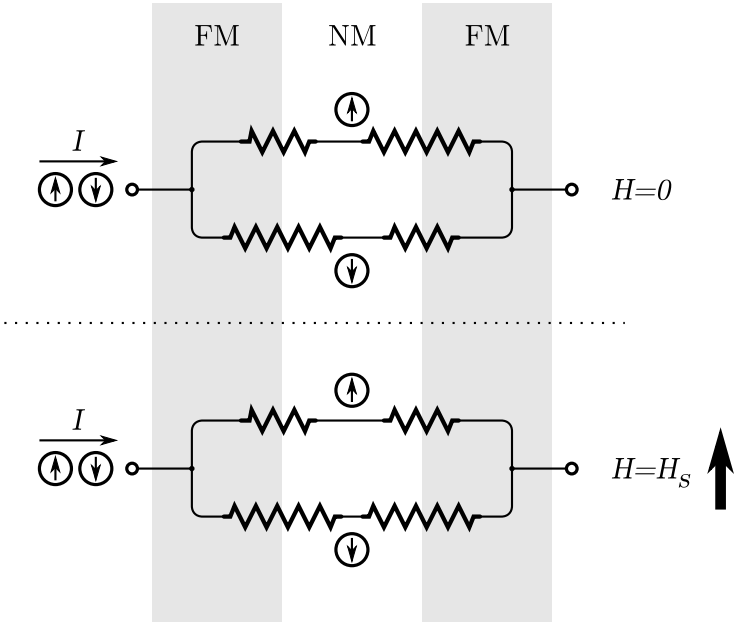

Figure 2.3: The two channel–two series resistor model for an initially antiferromagnetically coupled trilayer structure. The top row combined with the background colour shows the different metallic zones: here FM stands for "ferromagnet" and NM stands for "non-magnet". The second row shows how the scattering of both the majority (spin up channel) and minority (spin down channel) electrons will give contributions to those channels' resistances. The third row shows the low resistance case where an external field $H = \pm H_S$, where H_S is the saturation field, aligns the two ferromagnetic layers so that the majority carriers are scattered less at the metallic interfaces while the minority carriers are more strongly scattered at both interfaces.

A common realization of the GMR structure is the *spin-valve*, having important applications in modern technology. The spin valve structure is essentially a four layered device with two ferromagnetic layers separated by a thin non-magnetic spacer where one of the ferromagnetic layers are pinned by an antiferromagnetic layer through the exchange bias (see § 2.2). Assuming a ferromagnetic coupling between the two FM layers, the initial state of the system is that of low resistance. The high resistance state can be reached by applying an external magnetic field. The field must be sufficiently large to switch the unpinned layer to the antiparallel alignment, but smaller than the exchange field in the AFM–FM layers. If the field amplitude is increased past the exchange field, both FM layers will have been flipped giving a second low resistance state. The spin valve can thus be used to study both GMR and exchange bias, making it a very powerful and important magnetic structure.

2.5 The Spin Transfer Torque effect

The GMR effect, allowing manipulation of electrical resistances by an applied external field, has had tremendous technological importance. Conversely, Slonczewski[31] and Berger[3, 4] independently predicted that a spin-polarized current can be used to manipulate magnetizations, and hence mangetic fields. This effect is called *the spin-transfer torque* (STT) effect. In short, STT can be explained by the partial deposition of spin-polarized electrons' spin angular momentum into a FM layer. The deposited angular momentum will then alter the magnetization of the FM layer's.

In the following section the STT effect is described in more detail, starting with a semiclassical description of magnization dynamics, followed by a treatment of Slonczewski's modifications.

2.5.1 The Landau–Lifshitz–Gilbert equation

The *Landau–Lifshitz–Gilbert* (LLG) equation is a general equation of motion for magnetic moments in external magnetic fields. It can be deduced as follows[2]: a ferromagnet with magnetization $\boldsymbol{M}$ in an external field $\boldsymbol{B}$ will experience a torque per unit volume, $\boldsymbol{\tau}$, of $\boldsymbol{\tau} = \boldsymbol{M} \times \boldsymbol{B}$. Angular momentum, $\boldsymbol{L}$ is related to magnetic moment $\boldsymbol{\mu}$ via the gyramagnetic ratio: $\boldsymbol{M} = \gamma \boldsymbol{L}$, where $\boldsymbol{M}$ is the magnetic moment per unit volume. Since Newton's second law states that torque is the time rate of change of angular momentum, the magnetization (magnetic moment per unit volume) is directly related to the torque experienced by the ferromagnet:

$$\boldsymbol{\tau} = \frac{\mathrm{d}\boldsymbol{L}}{\mathrm{d}t} = \frac{1}{\gamma}\frac{\mathrm{d}\boldsymbol{M}}{\mathrm{d}t} \ . \tag{2.5.1}$$

If we insert the expression for the torque on the magnetization we end up with:

$$\frac{\partial \boldsymbol{M}}{\partial t} = \gamma \boldsymbol{M} \times \boldsymbol{B} \ . \tag{2.5.2}$$

[2]Landau and Lifshitz' approach was more elaborate than this, but this gives a nice intuitive picture of the relation

The equation above gives rise to a precession of the magnetization around the external field direction. From experiment we know that the magnetization will relax towards the field axis. To accomodate this Landau and Lifshitz[19] introduced a phenomenological term containing the repeated cross product of the magnetization with the field. This term acts to align the magnetization with the field axis.

$$\frac{\partial \boldsymbol{M}}{\partial t} = \gamma \boldsymbol{M} \times \boldsymbol{B} - \frac{\gamma\lambda}{M} \boldsymbol{M} \times (\boldsymbol{M} \times \boldsymbol{B}) \ , \tag{2.5.3}$$

where λ is the dampening strength[20]. A slightly different form was in 1955 proposed by Gilbert[14]. His term, later shown to be equivalent to the original dampening term[20], gives the LLG equation:

$$\frac{\partial \boldsymbol{M}}{\partial t} = \gamma \boldsymbol{M} \times \boldsymbol{B} + \frac{\alpha}{M} \boldsymbol{M} \times \frac{\partial \boldsymbol{M}}{\partial t} \ , \tag{2.5.4}$$

where α is the Gilbert dampening parameter[28].

If we now consider the angular momentum to be carried by quantum mechanical spin-1/2 particles (ie. electrons), then γ will be given by $\gamma = -\frac{g\mu_B}{\hbar}$, where μ_B is the Bohr magneton; $g \simeq 2$ is the gyromagnetic factor for electrons; and the minus factor comes from the fact that magnetic moment and spin point in opposite directions for electrons.

2.5.2 The Spin-transfer term

Slonczewski predicted that spin polarized electrons travelling from the pinned layer in a spin-valve to the unpinned layer will deposit parts of it's angular momentum there. As angular momentum is related to a magnetic moment, the deposition will modify the magnetization of the unpinned layer. If the spin polarized current comes from the pinned layer, the current will be polarized in the direction of the magnetization of that layer. Slonczewski showed that this current will act to turn the magnetization of the unpinned layer towards that of the pinned layer. If a current is sent in the reverse direction, with electrons being spin polarized by the unpinned layer, the opposite will happen. This is due to the minority electrons exiting the unpinned layer will be strongly scattered at the interface between the non-magnet and the pinned FM, making them return to the unpinned FM layer. The impact on the magnetization of the unpinned layer can be described by an addition of an extra term to the LLG equation; much in the same form as the dampening term, but with explicit dependency on the current and the misalignment between the two FM layers:

$$\left.\frac{\partial \boldsymbol{M}}{\partial t}\right|_{\text{STT}} = \frac{\eta(\Theta) I}{e\mathcal{V}} \hat{\boldsymbol{M}} \times (\hat{\boldsymbol{M}} \times \hat{\boldsymbol{M}}_{\text{fixed}}) \ , \tag{2.5.5}$$

where $\mathcal{V}$ is the volume of the region of the unpinned FM layer where the angular momentum is deposited; $\boldsymbol{M}_{\text{fixed}}$ is the magnetization direction of the pinned FM layer, I is the spin polarized current, and $\eta(\Theta)$ is a function of the misalignment Θ between the two net magnetizations. This term comes as an extention to the full LLG equation. As Eq. (2.5.5) has a similar form to the last term of the LL

equation, and thus implicitly the same form as the Gilbert dampening term. If the current is negative, then the STT term will act to destablize the precession of the magnetic moment. Solving for the equality between the Gilbert term and the STT term results in two critical currents: one for switching from the parallel alignment $\Theta \simeq 0$, and one for switching from the antiparallel alignment $\Theta \simeq \pi$.

A real ferromagnetic layer will in the general case not act as a macromagnet, so it is reasonable to expect metastable states before full switching. In these states the magnetic domain will precess at a high frequency determined by the current. As pointed out by Slonczewski[31], with reasonable material parameters, this can provide frequencies up to $\nu \sim 10$ GHz for currents around $I_C \sim 10^6$ A/cm^{-2}. This creates the possibility of using a direct current to create a high frequency transmitter or antenna, with possible applications in eg. inter–chip communication systems in integrated systems.

2.5.3 STT in Antiferromagnets

It was recently reported that not only ferromagnetics are affected by spin-transfer, but also antiferromagnets[37, 34]. The spin polarized currents will not only affect the magnetized domains, but also the local moments of the lattice sites in antiferromagnets[16, 42]. This can be seen in spin valve structures through a change in the exchange field. Wei et al.[37] reported on a changing exchange bias in a FeMn/CoFe/Cu/CoFe spin valve structure, here with CoFe as the ferromagnetic layers; FeMn as the antiferromagnet and the Cu as the non-magnetic layer. They observed a change in the field strength needed to overcome the exchange field as a function of the applied current. The slant in the exchange field vs. junction current curves showed a linear relationship, which can not be explained by conventional effects. Wei et al. attributed the change to local rotation of the antiferromagnetic moments due to a spin-transfer.

Chapter 3

Experimental Setup

3.1 Scanner design

The scanner I have used was designed by Magne Saxegaard, a PhD-student in the STM group at the department of physics, NTNU. As shown in Figure 3.1, the scanner is based on the use of cylindrical piezoelements (see § 2.1.2) for the positioning of the tip. The piezoelements are of different diameters ($OD_{\text{outer}} = 6.35$ mm, $OD_{\text{inner}} = 3.18$ mm), allowing them to be mounted concentrically. The piezoelectric tubes have voltage–displacement coefficients of:

$$\Delta Z = 17.3 \text{ nm/V} \tag{3.1.1}$$

$$\Delta XY = 129.75 \text{ nm/V} . \tag{3.1.2}$$

One end of the outer tube supports the inner tube via a ceramic (macor) ring, while the other end is fixed to the scanner's housing. This design increases thermal stability, as thermal expansions of the two tubes tend to cancel out eachother. In addition to the this, the compact design of this concentric STM (CCSTM) provides good vibrational stability, and can easily be fitted within the small gap of a convential two-coil electromagnet.

Coarse motion is realized with an inertial slider mechanism. A heavy tungsten (W) tip (Ø0.75mm) is fitted with an inverted spring made out of copper beryllium (CuBe) wires (Ø0.25mm) and placed on the inside of a small quartz capillary ($OD = 2.2$ mm). The cappilary is attached to one end of the inner piezoelectric tube. The tip is moved by applying a cycloid voltage waveform[29] across the inner and outer electrodes of the inner piezoelectric tube. A single strand of CuBe wire is glued to the inside of the quartz cappilary, acting as a sliding electrical contact with the tip–spring wires.

3.1.1 Enclosure and sample holder

The scanner is built around a base aluminium cylindrical container ($OD = 100$ mm, $H = 50$ mm, cf. Figure 3.2. The container has a center hole bored out where a copper cylinder is inserted. The copper cylinder has a radius of $r = 10$ mm and is extending 28mm from the base.

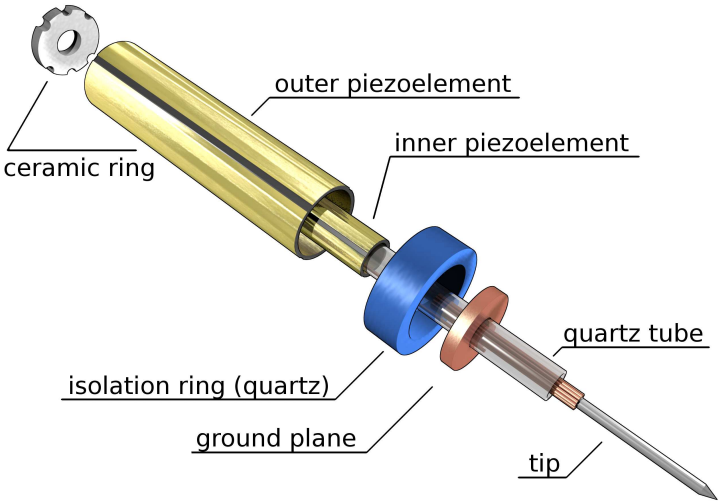

Figure 3.1: Exploded view of the inner parts of the scanner. The figure shows from left to right: 1. the ceramic (macor) plastic end cap (with cutouts for wires) used for connecting the two piezotubes together, 2. The concentrically aligned piezoelectric tubes, 3. the electrically insulating quartz (shown in blue), 4. the sample side ground plane, 5. the quartz glass tube, and last, 6. the tip connected to the copper springs lying inside the quartz tube. There is a copper wire running down the inside of the quartz tube, making sure that a electrical contact can be made to the tip and springs. On the piezoelectric tubes the electrode areas can be seen, both on the outside of the tubes and on the inside.

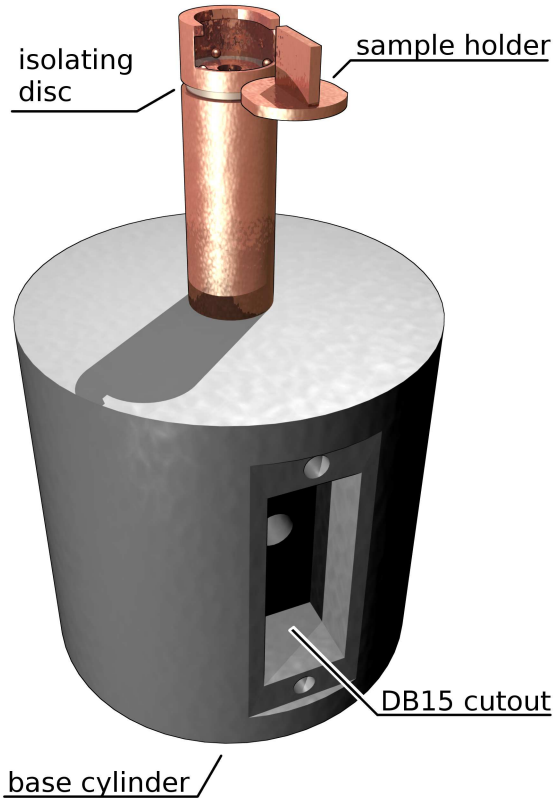

Figure 3.2: Scanner housing showing the base aluminium cylinder with the DB15 connector cutout. On the opposite side (away from viewing direction), there are two SMC coaxial outputs connected to the tip and sample side of the STM respectively. The insulating disc sitting between the copper tower cylinder and the scanner's head structure is shown in a a pale color and can be seen as a score around the tower cylinder. On the right the sample holder is shown hovering at the height at which it would be inserted into the scanner head.

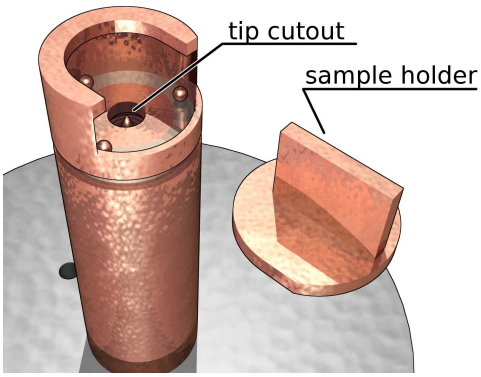

Figure 3.3: Closeup of the top part of the STM unit's tower, showing the sample holder (floating in the air), the top insulated portion of the sample housing and the cutout where the tip, glass tube and piezoelectric cylinders are placed. The image shows the small balls that the sample holder is resting on, but the springs holding the sample holder fastened have not been included in the rendering. The image is a rendering based on the CAD model containing the design used for manufacturing of the STM housing.

The outer piezotube is attached inside the copper cylinder with the top end epoxied to a electrical isolated quartz ring that is attached to the top edge of the cylinder. That way, the piezoelement configuration is concieled within the copper cylinder providing both electrical shielding as well as physical protection. Electrical leads connecting to the piezotubes' electrodes run down the inside of the copper cylinder and into the base aluminium cylinder where they are presented at a DB15 terminal for easy connection (see Figure 3.2).

The isolating ring is epoxied between the top edge of the copper cylinder and the scanner head. The scanner head is the part where the sample is held. The scanner head has a slot for inserting a copper disc on which the samples are to be attached (see Figure 3.3). The samples can be attached to the copper disc by means of a rather large metal flap acting as a retention spring, or by gluing it in place by using an electrially conducting epoxy. When inserted into the scanner head, the sample holder has a clearance of a few millimetres to the top the inner glass tube lying flush with the top edge of isolating ring and a copper disc acting as a shielding ground plane. This design is a tight fit, but will still allow the user to insert the sample holder without damaging the tip. The main advantage of keeping everything so compact is that the course motion auto-approach times can be kept to a sensible small period, and that the entire scanner head can be mounted inside a conventional electromagnet.

The sample holder and the tip is electrically insulated from eachother, but electric leads run from both the tip and the sample to coaxial output ports on the base of the scanner's outer metallic enclosure.

To improve signal to noise ratio, a hollow, capped aluminium cylinder with a bore just large enough to accomodate the STM tower is manually placed on top of the STM. The aluminium cylinder is insulated on the inside by a thin

plastic film as not to make accidental contact with any metal parts on the STM tower. Since the capped aluminium cylinder is in electrical contact with the base aluminium cylinder it acts as a radiation shield for the circuit, lowering the impact of radiation noise by a substantial amount.

3.1.2 Electromagnet

Since the STM unit is mounted in a rather long cylinder with a small radius, the unit can conveniently be inserted into an electromagnet. The electromagnet we use is a set of two wound coils with $N \simeq 850$ windings each, separated by a distance just large enough to slide the STM "tower" inbetween (see Figure 3.4). The electromagnet is connected to a high performance voltage controlled current source, a Kepco BOP 100-10MG capable of both sinking and sourcing of 10 A at 100 V up to frequencies of 4 kHz. At the maximum current of 10 A, the coils put out a field of $H \simeq 100$ mT in the center region.

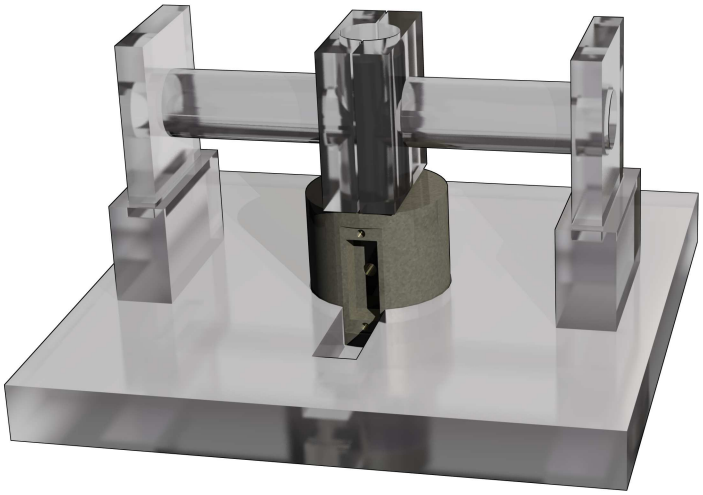

Figure 3.4: Rendering of the base setup, showing how the STM unit is placed within a base made out of acrylic glass. The fit between the different parts is so tight that the system acts as one unit. The figure also shows the horizontal acrylic cylinders encapsulating the STM's tower unit and aluminium shielding cylinder. These acrylic cylinders are wound with $N \simeq 850$ windings each providing an powerful electromagnet as part of the system. This whole unit is made to rest on a foam or rubber mat, to improve vibration dampening.

3.1.3 Coarse motion and auto-approach

If a tube is expanded in an accelerated manner and then suddenly taken to a halt, the copper leafs of the tip holder pressing against the glass surface will transition from static to sliding friction. This is commonly referred to as an

"inertial slider" mechanism, and is often utilized for coarse motian in *scanning probe microscopes* (SPM)[39]. By a clever selection of the way the voltage is ramped over the outer piezo tube, this throwing mechanism can be used in a predictable and reproducible manner.

To go from a non-contact to a stable tunneling contact, the tip has to be moved toward the sample surface while monitoring the tunneling current. In our system, this is done by ramping the voltage over the inner piezotube's electrodes. If a tunneling current is not "found" within the ramp signal's range, the piezotube is contracted slowly back to it's starting position and then a throw is performed by the method described above. Then the voltages are ramped yet again while searching for a tunneling current. This is performed in an incremental manner until a stable tunneling current has been achieved within the middle range of the voltage ramp. The coarse motion control software then switches to a holding mode where the applied voltage is regulated with a conventional PI negative feedback controller, comparing the amplified tunneling current signal with a user defined setpoint. This means that the tip can be kept at a approximate constant distance from the sample surface.

3.1.4 Scanning

Once the tip has been brought into tunneling distance, the software can be switched to scanning mode. In scanning mode the inner piezotube is kept at the same voltage as that found by the coarse auto-approach, but this time the voltage is kept constant while a PI regulator is applied to the outer piezotube. The differences in the sizes of the two piezotubes manifests itselves as different relations between the applied voltages and the change in spatial changes of the tubes. Another advantage of using two piezoelectric tubes is that we can use different gains on tubes' control signals, giving different vertical resolutions. This way we can achieve good resolution on the scan tube, while still having the possibility of a large travel on the inner coarse tube.

This is where this scanner design has it's main advantages. You can achieve fast and accurate coarse motion while still having the possibility of doing finer regulation during scanning.

By ramping the voltages on the electrodes of the outer piezotube, effectively bending it, while still regulating it's expansion and contraction, the tip can be swept linewise over the sample at an approximate constant separation distance. If one samples the voltages applied by the PI regulator, a raster image of the sample surface can be taken.

3.2 Hardware

The scanner can be operated in two measurement modes and three software control modes. The two measurement modes is the *STM mode*, and the *Point Contact* (PC) mode. In the STM mode there are two different software control modes: "coarse"- and "scan"-mode. The PC measurement mode has only one software mode assosciated with it, called "PCS". The two measurement modes can be selected by toggling two digital input signals on the signal splitter board, which will switch two relays in a complementary fashion. The different purpose built electronic boards used in the different measurement modes will be described in the following sections. See Figure 3.5 for an overview of the components discussed in the following sections, along with these components interconnections.

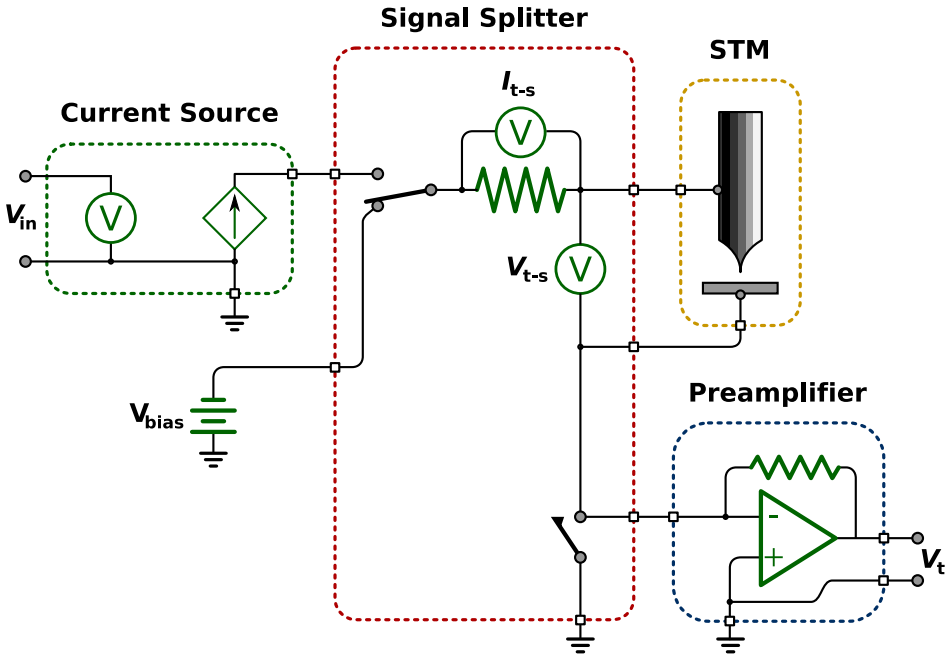

Figure 3.5: Showing the interconnects between the different hardware components. The splitter board can be used to switch between the current sender (vccs) and a voltage source (V_{bias}). The splitter board can also couple the sample side to ground, eliminating the preamplifer as the current drain. The two voltage probes on the splitter board are used to measure the current through, and the voltage over the tunneling junction; here depicted in the STM unit.

3.2.1 Tunneling Current Preamplifier

In the STM mode a relay on the splitter board couples the tip side of the scanner to an external voltage channel while the sample side of the STM junction coupled to the *tunneling current preamplifier*. The preamplifier has been designed and built by the guest researcher Bernt M. Førre at the department of physics,

NTNU. The input signal to the preamp, ie. the sample side, is kept at virtual ground, and the tunneling current is forced to flow through a large shunt resistor, converting the current signal to a voltage signal. By virtual ground I mean that the lead comming from the sample side of the scanner is tied to the inverting input of an operational amplifier while the noninverting input is tied to ground. By connecting a large shunt resistor (100 MΩ) from the inverting lead to the output lead of the operational amplifier the tunneling current caused by the bias voltage and the small tip–sample separation distance can be measured. This configuration is the well known inverting amplifer where the input resistor has been removed (alternatively it can be viewed as a voltage summer with only one input). To be able to measure the tunneling current of, typically, only a few nano amperes, it is essential that the input bias current of the operational amplifer is as small as possible. The input bias current is a driving current going into the inverting and noninverting inputs of the operational amplifier, This can only be achieved with very high input impedance operational amplifiers, thus the operational amplifier chosen is therefore a FET based operational amplifier with GOhm input impedance.

3.2.2 Current sender

When performing GMR and STT related point contact measurements, we want to control the applied current through the contact rather than the bias voltage. One can apply a sufficient bias voltage to get a current in the approximate correct range, but since the point contact resistance can vary substantially from one contact to the next, the method of applying a bias voltage is not viable. I have therefore created, as part of this thesis work, a current sender capable of delivering a current in the range ±33 mA that can be controlled directly by an analog voltage, V_{in}, in the range $V_{\text{in}} \in [-10, 10]$ V.

The current sender has a voltage level conditioning stage followed by a current delivering stage. The current delivering stage was built by using a differential instrumentational amplifier with a voltage divider with the center fed back to the instrumentational amplifier by means of positive feedback (see Figure 3.6).

The negative lead of the differential amplifier is tied to ground, so the only voltage on the output is given by the noninverting input. The output of the differential amplifier is connected to the high speed buffer chip, BUF634, that can source and sink up to 250 mA, with a bandwidth up to 30 MHz. The buffer chip is used because the differential amplifier alone can not deliver large enough currents for our measurement needs. The drawback with the buffer is that it has a rather large, but slowly varying voltage offset. So, as the data sheet of the BUF634 states, it has to be included within a negative feedback loop to remove the error. This was done by connecting the output of the buffer to the instrumentational amplifier's SENSE pin, which is internally connected to the inverting input via a 25 kΩ resistor.

The output of the buffer chip, matching the voltage output of the instrumentational amplifier, due to the negative feedback discussed in the last section, is then fed down to a calibration resistor (R3 in Figure 3.6) in series with the

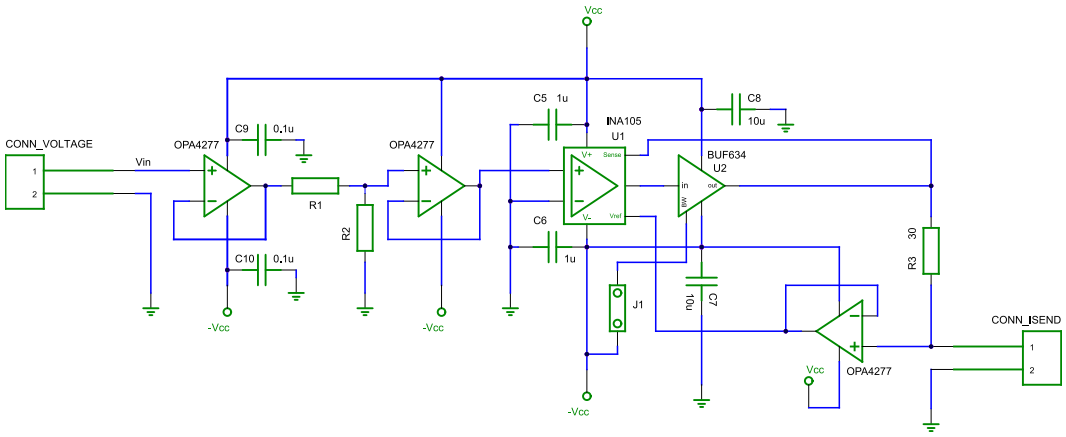

Figure 3.6: Schematic for the current sender circuit. The input control voltage is given on CONN_VOLTAGE, while the load resistance is connected to the two terminals of CONN_ISEND. J1 is a selectable jumper for toggling between low bandwidth (default) or high bandwidth mode on the high speed buffer chip. ±Vcc is usually set to ±15 V, while R1 and R2 is set up to provide a 10:1 attenuation.

applied load; in our case the STM tip–sample junction. A voltage tap between the calibration resistor and the load is then fed through an additional operational amplifier acting as a voltage follower to the REF pin of the instrumentational amplifier. The REF pin of the instrumentational amplifier is equivalent to the noninverting input lead, so any applied voltage there will be added to the output of the buffer. The feedback of the voltage between the resistances is therefore supplying the system with positive feedback which act to keep the current through the load constant.

Since the feedback is done via an opamp as a voltage follower, the current is effectively delivered directly to the load and not to the REF pin of the instrumentational amplifier. The opamp is also making sure that the matched resistor network of the instrumentational amplifier will remain matched, as the output impedance of the opamp is small enough to not adversally effect the common mode rejection of the instrumentational amplifier.

The voltage conditioning stage on the input of the current sender circuit is there to scale the input voltage to a suitable level so as to give the buffer and instrumentational amplifier chip combination enough voltage headroom for the current regulation. A suitable configuration was to attenuate the signal by a factor of 10 as preconditioning. A voltage in the range $[-10, 10]$ V applied to the current sender's input will then, after circuit analysis based on the operation of ideal operational amplifiers, give a current through the load of:

$$I = 0.0033 V_{\text{in}} \ , \quad V_{\text{in}} \in [-10, 10] \text{ V} \ . \tag{3.2.1}$$

The buffer chip is capable of driving the combined resistance of the load and calibration resistor up to a voltage of (worst case) $(V^+) - 2.1$ V and $(V^-) + 2.1$ V,

where $V^{\pm}$ is the positive and negative supply voltage that the buffer is driven from. $V^{\pm}$ is typically set to ± 15 V in our case, but can easily be extended to allow larger currents. Since I am using the INA105 as the instrumentational amplifier, driven from the same supply rails as the buffer chip, the maximum output voltage will actually by limited to typical 13V nominal and 10-12V worst case. This means that with a calibration resistance of $R_{\mathrm{C}} = 31\ \Omega$ this sets a restriction on the maximum load resistance we can do measurements on, given that we want to supply currents up to 33 mA, we can drive resistive loads up to a maximum of:

$$\begin{aligned} R_{\mathrm{max}}^{\mathrm{load}} &\approx \frac{U}{I_{\mathrm{max}}} - R_{\mathrm{C}} = \frac{12\ \mathrm{V}}{0.033\ \mathrm{A}} - 31\ \Omega \\ &\approx 332.6\ \Omega\ . \end{aligned} \tag{3.2.2}$$

This should be enough for achieving rather large current densities in point contacts on metallic samples.

Before manufacturing the printed circuit board for the current sender the circuit was simulated using Spice. I used the Spice3-models supplied by Texas Instruments for the different integrated circuits in Figure 3.6 as building blocks in my Spice simulation netlist. By writing a batch-program in python that wrote parts of the netlist parameters, I could iterate over different circuit parameters. This made it possible to quickly find suitable values for the precondition resistive divider and the calibration resistance. Figure 3.7 shows the output from such a batch simulation with input parameters in the wanted range.

3.2.3 Signal Splitter

I built the new *relay splitter board* to able to utilize the virtual ground configuration preamplifier while still making it possible to switch to a point contact measurement mode, using the current sender circuit is needed. The splitter board is controlled by two digital signals. The two digital signals are used to control three 5 V Meder SIL-05-1A72-71D relays, having a coil resistance of 500 Ω, thus requiring a driving current of 10 mA. The relays have a switching time of up to 1 ms. Since this, in the general case, is quite a lot of current for ordinary digital output pins, I chose to use bipolar junction transistors (2N3904, npn type) to drive the relays from the splitter board's internal digital 5 V supply. I used two relays to build a *single pole, double throw* digitally controlled switch. One of the digital input lines is connected parallely via 4.7 kΩ resistors to the bases of two different transistors. This gives a required current drain of

$$I = 2\frac{5.0\ \mathrm{V}}{4.7\ \mathrm{k}\Omega} \approx 2.1\ \mathrm{mA}\ ,$$

ten times less than the original requirement. One of the relays is connected between the +5 V rail and the collector, with the emitter connected to digital ground. Thus, the first relay will be turned off if the digital line is pulled low (0 V). The other transistor has a 2.2 kΩ resistor between the collector and the

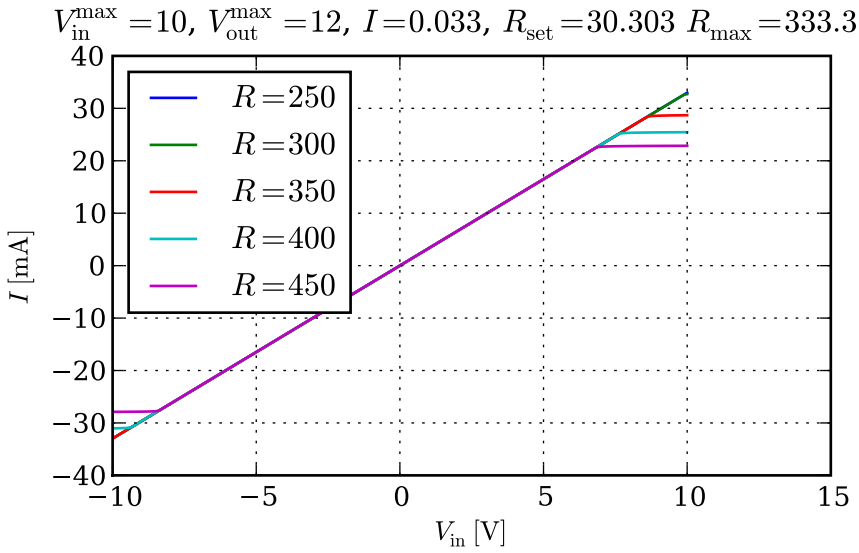

Figure 3.7: Batch output of the current sender circuit simulated using Spice. Delivered current as a function of applied input voltage for different sizes of load resistance. An input stage attenuation of 10 was chosen, with an input voltage in the range ±10 V, a maximum expected current for $V_{\text{in}} = 10$ V of 33 mA. The simulation was performed assuming a maximum output voltage of $V_{\text{out}}^{\text{max}} = 12$ V from the BUF634/INA105 chip combination.

+5 V rail, giving a TTL inverter configuration. The collector of this transistor is then connected to the base of a third transistor that drives the second relay. The second relay will therefore be active when the digital line is pulled low, and deactivated when the line is pulled high. The third relay is driven from a single npn transistor in the same way as the first relay, but from the second digital input line. See Figure 3.8 for a schematic capture of the circuit.

The splitter board contains a digital region containing the digital power supply, the transistor drivers and the driving sides of the relay. The rest of the board is on a totally isolated analog ground, only implicitly connected to the rest of the circuit via the relay. The analog side has two *SubMiniature version B* (SMB) input connectors that are attached to the first and second relay respectively. This way, the first digital control line can be used to switch between these two analog input signals. These lines are called VBIAS and ISEND, where VBIAS is normally active when the first digital line is pulled low. VBIAS is used to set a bias voltage over the tip–sample junction in the STM mode, while ISEND is used to connect in the current sender circuit in the PC mode (see § 3.2.2).

Furtermore, the line comming from the two complementary relays is then connected to an SMB output connector called RHIGH. Close to this output, there is an input channel called RLOW. An instrumentation amplifer is connected with the noninverting input connected to RHIGH and with the inverting input connected to RLOW. By connecting a resistor with a known resistance between the RHIGH and RLOW terminals, it is possible to measure the current through the

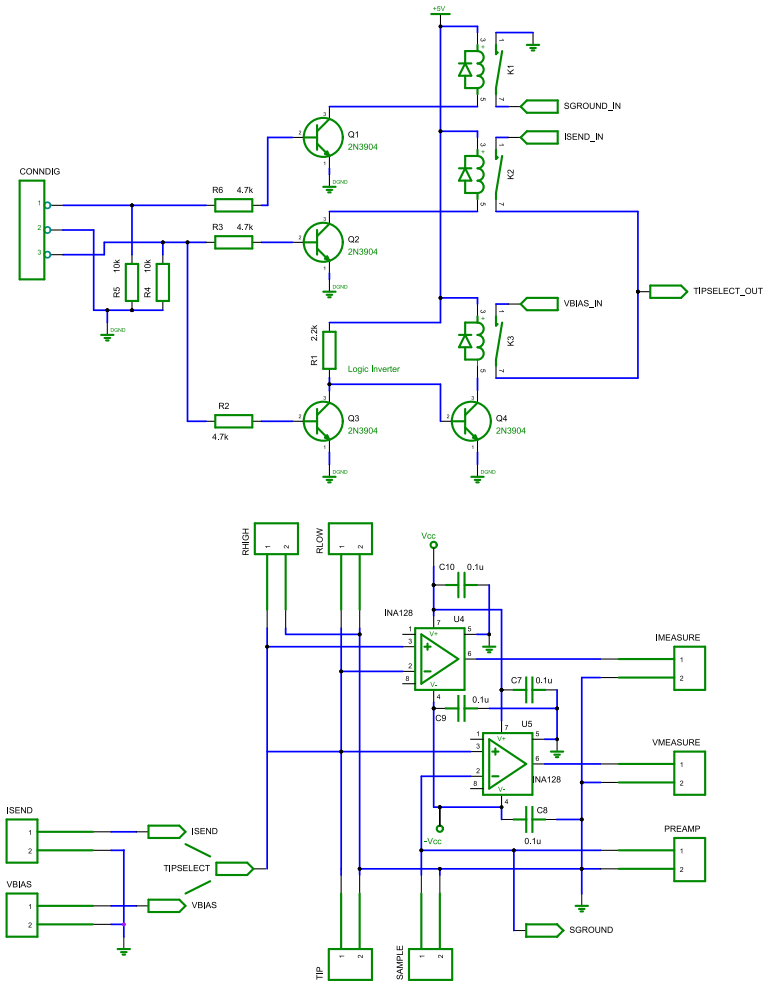

Figure 3.8: Electronics schematic for the splitter board. The output TIPSELECT_OUT is connected to TIPSELECT; VBIAS is connected to VBIAS_IN; ISEND is connected to ISEND_IN; and SGROUND is connected to SGROUND_IN. The instrumentation amplifiers have no resistor connected between pins 1 and 8, meaning that the are acting as unity gain amplifiers.

resistor. The instrumentation amplifier is an INA121 FET input, low bias current, amplifier chip that has a three–opamp differential input configuration. The output from the instrumentation amplifier is presented at a SMB output connector on the board called IMEASURE. The signal line is then further connected to the non-inverting input of a second instrumentation amplifer as well as an output SMB connector called TIP. This line will be externally connected to the tip side of the STM. An input connector called SAMPLE, externally connected to the sample side of the STM, is then fed to the inverting input of the second instrumentation amplifier, to an output connector called PREAMP, and to the third relay. The output of the second instrumentation amplifier is presented at an output called VMEASURE, giving the possibility of measuring the voltage drop over the tip–sample junction in the STM. By sampling the two voltages coming from the instrumentation amplifiers simultaneously and taking the quotient between the tip–sample voltage and the current sensing voltage, the junction resistance can be calculated. Thus, the system provides a direct method of resistance measurements in the PC mode.

The output called PREAMP is normally externally connected to the input of the tunneling current preamplifier (see § 3.2.1), thus pulling this connection to virtual ground in the normal operation, STM, mode. To avoid risking over-current induced damage to the preamplifier, the third relay can be activated to connect the sample side directly to analog ground. A proper change to the PC mode involves first switching the sample side to ground, switching out the preamp, before switching in the current sender.

As mentioned above, the ground planes of the digital circuitry and the analog components are completely separated. This is to inhibit digital switching noise from infering with measurement signals. Furthermore, all three printed circuit boards (the preamp, current sender and the splitter board) has been built into a metal enclosure to further improve noise immunity. All the SMB connectors on the different boards are presented at the enclosure's front and back panels, with all the connector shields connected to the enclosure. Whereever it has been possible, I have tried to follow the connection rules and advices given by Vasilescu[35], as to keep noise and interferring signals away from the STM measurement signal line.

3.3 Software

The system used for controlling the STM consists of a *field programmable gate array* (FPGA), a National Instruments PXI system (NI PXI-8187) and a standard desktop personal computer. The FPGA is responsible for the direct control of the STM scanner's piezotubes; the PXI system is responsible for coordinating the FPGA's activities with those of the user: making measurements, setting system parameters etc.; and the desktop personal computer is used for displaying the host program to the STM operator and for doing postprocessing on gathered data. The different components of the system will be described in the following sections.

3.3.1 PXI Host system software

The host system of the FPGA control module is a *PXI*-based *National Instruments* (NI) computer system. A PXI bus is an extension to the PCI (Peripheral Component Interconnect) computer bus often used in ordinary desktop computers of the last decade. The abbrieviation stands for **P**CI e**X**tensions for **I**nstrumentation. The PXI specification is a hardware specification based around the CompactPCI form factor with additional rules for interconnection between modules within the system[27][24].

In our PXI system (NI PXI-8187) we are using three extension cards. These are apart from the main motherboard module which also comes in the same form factor as the PXI extension cards. The modules are:

- A multifunction DAQ (data aquisition) (NI PXI-6259) card featuring four analog 16 bit input channels, four 16 bit digital to analog output channels, 48 digital I/O lines and several trigger signal lines (mostly unused in our case).
- A high speed digitizer (NI PXI-5922), essentially a high speed DAQ, with two unbalanced coaxial input channels. Both channels can be used to aquire signals in the ± 5 V range up to a selectable resolution of 24 bits at up to 500 kSamples/s.
- The before mentioned FPGA extension card (NI PXI-7833R) features a Xilinx Virtex-II FPGA in a neatly packaged PXI module. The module features 8 16 bits analog input channels, 8 16 bits analog output channels and 96 programmable digital I/O lines. The FPGA module can be driven up to a frequency of 40 MHz, which, given an FPGA's parallel processing, gives a lot of freedom for developing the STM control signalling.

LabVIEW (The G Programming Language)

We are using the well known graphical *LabVIEW*$^{\text{TM}}$programming environment from NI. It is based on the graphical programming language G invented by NI, where the concept of "virtual instruments" or VIs is the key feature. A VI can be compared with subroutines or functions in other languages, where data flow can

be graphically wired between the VIs for defining program flow. The LabVIEW environment has support for almost all the normal programming techniques available in other languages. In many ways it can be thought of as a graphical "wrapper" of the C programming language.

One of the most important advantages with using the LabVIEW environment over traditional text based programming languages is NI's vast library of ready-to-use VIs and instrument drivers. This makes it alot easier to begin development for istrumentation projects. Sadly, one of the biggest problem with using LabVIEW is that the graphical programming gets problematic when the project gets to a certain size, as the "real-estate" space used by the program starts extending beyond the small space that a typical monitor can display. The biggest problems starts appearing when an already existing, large program needs altering. Since all program flow structures like loops and conditional branches are expressed as graphical containers for ordinary program blocks, resizing becomes a problem. This is because the program flow structures often are surrounded by supporting code that makes it hard, and time consuming, to alter the programs layout and sizing.

An alternative to using the LabVIEW environment is the LabWindows/CVI (C for virtual instruments) programming environment supplied by NI. As the LabVIEW VIs are mostly wrapped around existing C functions, this environment supplies the same kind of easy-to-use resources as the graphical LabVIEW environment, thus allowing the user to program all the instruments using ordinary ansi C. Since the development of the STM system described in this thesis was started several years ago based on the usage of the G programming language, I have stuck with it in the current work. This is partly because the codebase which I started working on would be non-trivial to reimplement in the LabWindows/CVI environment in the time window of this work. In relation to this the programmer's proverb "It is irrelevant to optimize non-working code", comes to mind.

A running LabVIEW VI is controlled through the graphical user interface (GUI) referred to as the "*front panel*". The front panel can be relayed through a network connection, allowing a remote PC system to display the program state of eg. a program running on the Real Time NI-PXI system discussed next.

LabVIEW Real Time functionality

On our PXI system we are using the "Real Time" operating system provided by NI together with the included real time capabilities of the LabVIEW VI library. The real time capabilities means that we can secure that the PXI host system can service the FPGA within a deterministic time, but in our case it is mostly used to allow sub-millisecond time resolution between certain events, and to force the host system's main software loop to a small period, typically around 1 ms.

Main software strategy

The strategy for our host system control software involves the use of two main loops, roughly corresponding to two software threads, running at two different speeds. The "fast loop" is responsible for controlling the main internal software

modes, controlling the external hardware modes related to the splitter board, initializing and administering the FPGA's modes as well as setting up and running the point contact measurements by means of the multifunction DAQ and high speed digitizer. The "slow loop" is responsible for saving all incoming measurement- and scan-data to disc as well as handle all network related activities.

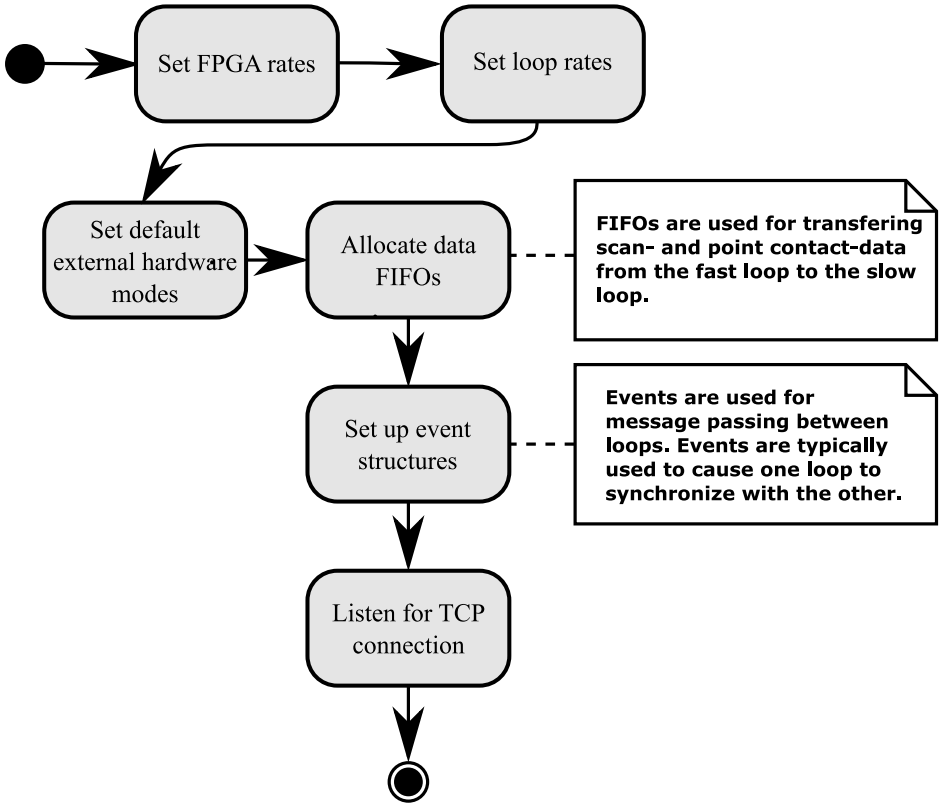

Figure 3.9: Initialization of the PXI host program. The rates determine the ideal running speed that the FPGA, fast loop and slow loop should have. Typically the slow loop runs some hundred times slower than the fast loop. The TCP initialization step is only used if the user wants to stream the scan data raster image to some network connected host computer.

Figure 3.9 shows the initialization step of the host program. Here all network connectivity, inter-loop communication channels and buffers are set up. There is also a step where all the external digital control lines are (re)set to the default STM-configuration. That step ensures that the program can be restarted after being stopped in a state differing from the normal STM operation.

Figure 3.10 shows the interplay between the two loops. The fast loop's main activity involves selecting and running the appropriate software operating mode given the user's selection and the internal state of the current operating mode. At certain key points during a software mode's state execution there is a need for synchronizing with the slow, data handling loop. The synchronization usually involves sending a signal, perform some action and then at some point start

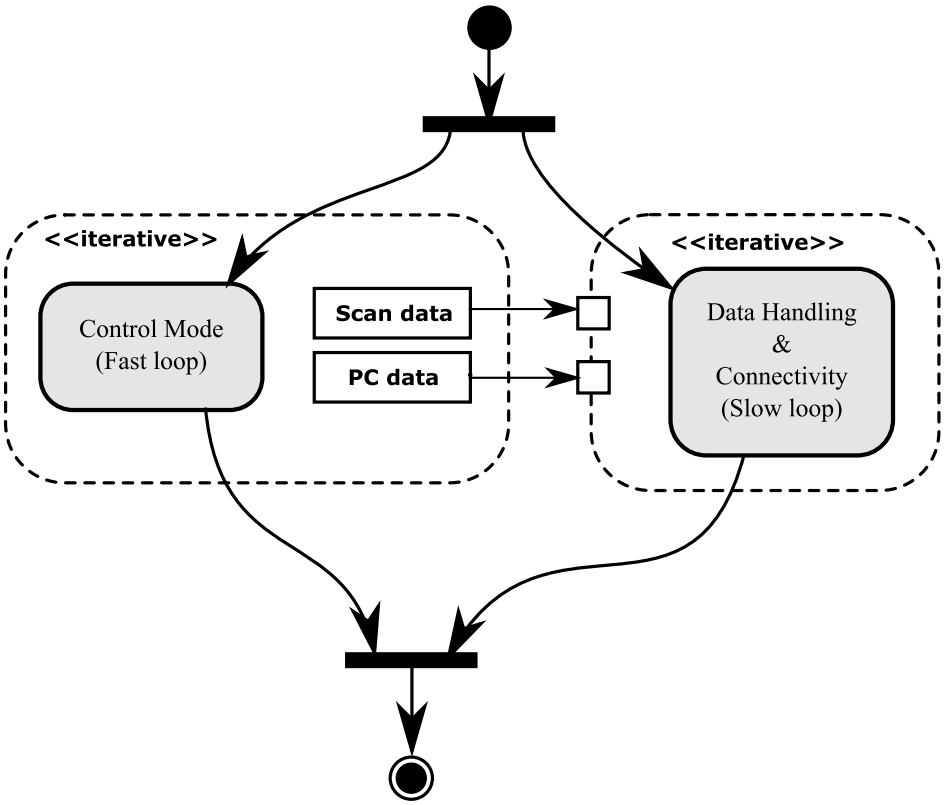

Figure 3.10: Fast–Slow loop interplay. The data generated by the FPGA are downloaded by the fast loop and sent, via a first-in-first-out pipe, to the slow loop for accumulation and saving to disk.

waiting for an acknowledgement from the slow loop by entering a strict substate where the main task is to poll the return FIFO.

In our system the signals are implemented as user defined events that upon creation, are relayed to the slow loops event queue where it will be taken care of by the slow loop's event structure at the next iteration of the slow loop. The fast loop, on the other hand, does not contain an event structure, so acknowledgements have been implemented using a one-element boolean real time FIFO. The advantage of using a FIFO in stead of more regular synchronization mechanisms like mutexes or semaphores is that after the one element sized FIFO has been read from, subsequent reads will not return a result. This way we can avoid the fast loop blocking in the synchronization, thus still making it possible to continue servicing the user and FPGA.

The two loops also acts as regular producer–consumer loops. The fast loop can download scan data from the FPGA or it can itself start some measurement creating an incoming data stream from eg. the high speed digitizer mentioned above. These data streams are then relayed to the slow loop by using multiple-element sized real time FIFOs. Real time FIFOs have a deterministic time-requirement for insertion and querying; they are fully specified in terms of size, before they can be used. The important difference between signals and data transfers is that data transfers **never** requires acknowledgements from the slow loop. This way, the fast loop can keep it's focus on servicing the FPGA while the slow loop will take in larger collections of data and save them to disc. Since the quotient between the loop rates of the two loops can be adjusted, the slow loop can be tuned to maximize disc throughput, reducing the total time the PXI spends on file saving.

Mode Control (Fast loop)

The fast loop is implemented as a statemachine running at a clock period of about 1 ms. The main responsibility is to select operating mode and run the activities corresponding to that operating mode's internal state, but it is also responsible for all user related controls, ie. taking actions based on the state of the host program's front panel. The first activity undertaken by the fast loop in each iteration is to poll the FPGA for information the microscope's current physical state. This information is then used for making later decisions as well as informing the user of the microscope's current state. The second activity is selected based on the current operation state. This activity involves servicing and controlling the current state of the FPGA, and as such, it's state is given by the same three software modes as described for the FPGA: coarse mode, scan mode and point contact mode.

The coarse activity is shown in Figure 3.11. As the coarse software mode is almost entirely implemented on the FPGA PXI module (see § 3.3.2) this activity on the PXI host system is mostly a control mode telling the FPGA what submode of the coarse motion to perform. That is, set the FPGA to either a paused state, an auto-approach state or make it perform some manual approach or retract

activity.

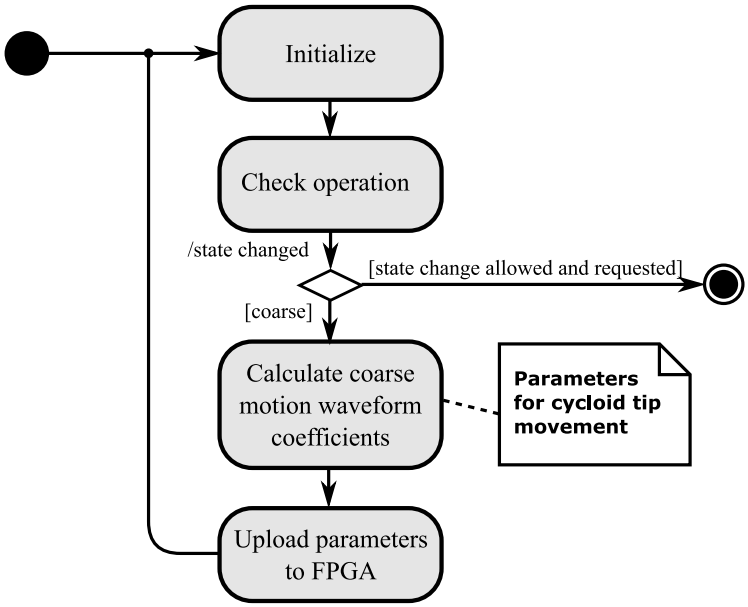

Figure 3.11: The coarse activity's internal flow. The last step also includes uploading the maximum amplitudes, coarse motion timescale, voltage output, max coarse motion voltage, the PI regulator's constants, the mode (manual retract/approach, pause, or auto-approach) and any single steps that user has requested. If the host program is told to shut down, a stop flag will be toggled telling the FPGA to turn all voltages down to zero in a controlled manner.

The scan activity is shown in Figure 3.12. As the figure shows, the state involves uploading new scanlines to the FPGA whenever the FPGA signals a data-ready by means of an interrupt request (IRQ) on one of the PXI system's IRQ-lines. The scan activity maintains it's own internal state, tracking the current scan line and taking decisions on wether software mode switches are allowed or not.

When the scan activity detects that a scan has completed, ie. the specified number of scanlines at the selected number of points per scanline has been completely scanned, the scan activity sends a "request restart" event signal to the slow loop. This is an important signal that tells the slow loop to finish saving all the data in the real time data transfer FIFO and then close the current file followed by creating a new file for the next scan. After sending the request-event signal to the slow loop, the fast loop goes into a state where it will poll for a "restart acknowledgement"-signal from the slow loop while still servicing the FPGA and user. Only upon receiving the acknowledgement from the slow loop, is the new scan started. This makes sure that all the data of the current scan frame are saved before a new scan can start.

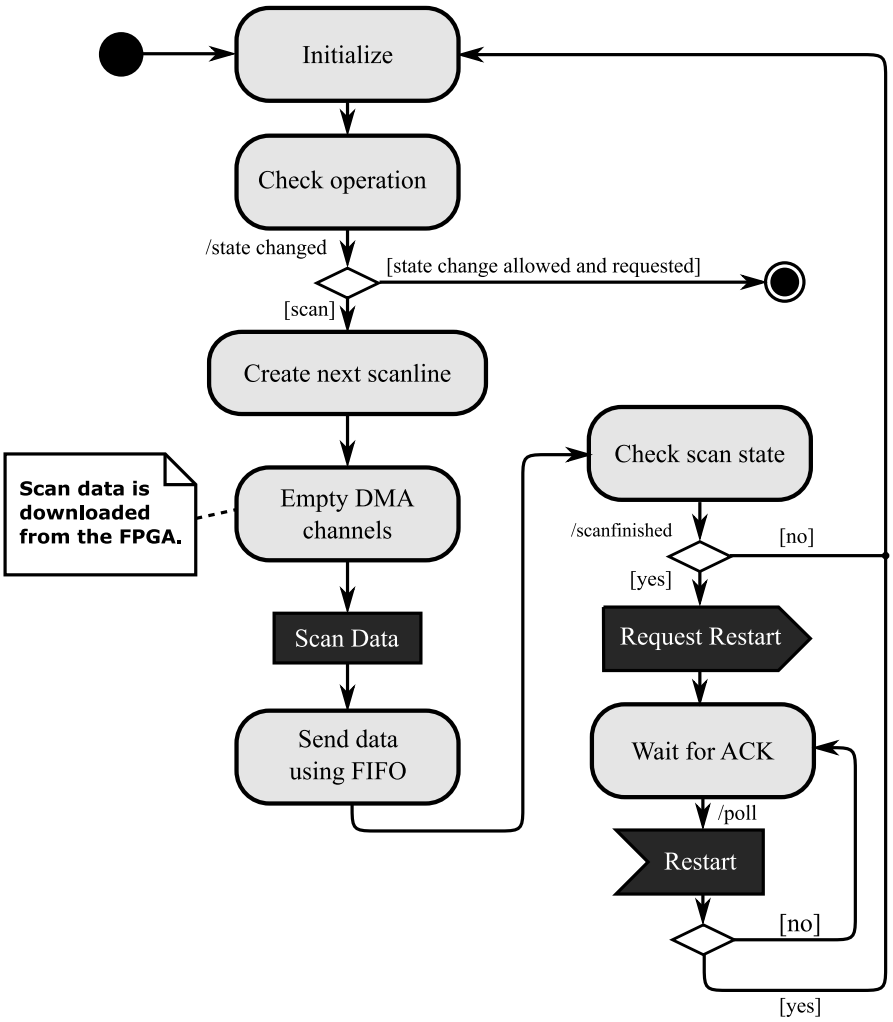

Figure 3.12: The scan activity's internal states. The initialize activity of the fast loop has been included as the first state for completeness. The rectangular black parts signifies the transition of an object, here the downloaded scan data, from one state to the next. The convex pentagon is an outgoing signal to the fast, by means of an event signal. The concave pentagon is an incoming acknowledge signal from the slow loop, here shown in the normal polling state.

The point contact activity is shown in Figure 3.13. As the figure shows, the activity starts with uploading the coordinate of where the point contact is to be performed. Since the scan mode on the FPGA includes the option of not uploading scan data for certain points this action is actually performed while keeping the FPGA in the scan mode. Only after the FPGA reports that a new scan point can be uploaded, done via an interrupt request (IRQ), do we change the mode on the FPGA. This is illustrated in the "Deactivate scan PI-regulator" action in Figure 3.13, which basicly is a mode change of the FPGA. The search current is user selectable, and can be chosen from a few μA to several mA.

Before starting the measurement, the multifunction DAQ is set up to source the two user selected waveforms for the current through the tip–sample junction and the magnetic field. The digitizer is set up to aquire samples at a user selectable sampling rate. We often "oversample" with the digitizer by using a sample rate as high as 100 kHz. This is to be able to do quite aggressive post processing on the aquired signals, by means of averaging and digital filtering. The multifunction DAQ is configured to start on a trigger signal supplied on the internal signal bus of the PXI-system. In our case the trigger signal will orignate from the digitizer, thus making sure that the aquisition is started just prior to the generation of the waveforms.

The measurement state of the point contact involves starting the digitizer, which will start the waveform generation. The data is then streamed from the digitizer, in much the same way that scan data are downloaded from the FPGA, and then delegated to the slow loop. Figure 3.13 does not include the explicit signal passing as Figure 3.12 has, but a "PCSstart" event signal is fired just before the measurement is started, and a similar poll state is implemented after the measurement has finished. The poll state has the same functionality as the one in the scan activity; making sure that all the measurement data is securely saved to disc before continuing with other tasks. This is vital for point contacts, especially when we are oversampling, as a sample rate of 100 kHz will generate almost up to a megabyte per second. The data extracted from the high speed digitizer is in 32 bit signed integer format for each channel, given that the aquisition is in done in 24 bit resolution. With a sampling rate of 100 kHz this gives us, assuming 8 bit bytes:

$$\begin{aligned} D &= 2 \cdot 4 \text{ B/S} \cdot 100 \text{ kS/s} && (3.3.1) \\ &= 800000 \text{ B/s} \\ D &\approx 0.763 \text{ MB/s} , && (3.3.2) \end{aligned}$$

where D is the data generation rate from the high speed digitizer sampling from two channels simultaneously, and the unit S means "Sample".

Data handling & connectivity (Slow loop)

The main responsibility of the slow loop is to save the incoming scan and point contact measurement data to disc. The data is saved in one binary file per scan frame, with the performed point contact measurements saved to parts of the same file. The a full file format description is given in Appendix A. The slow

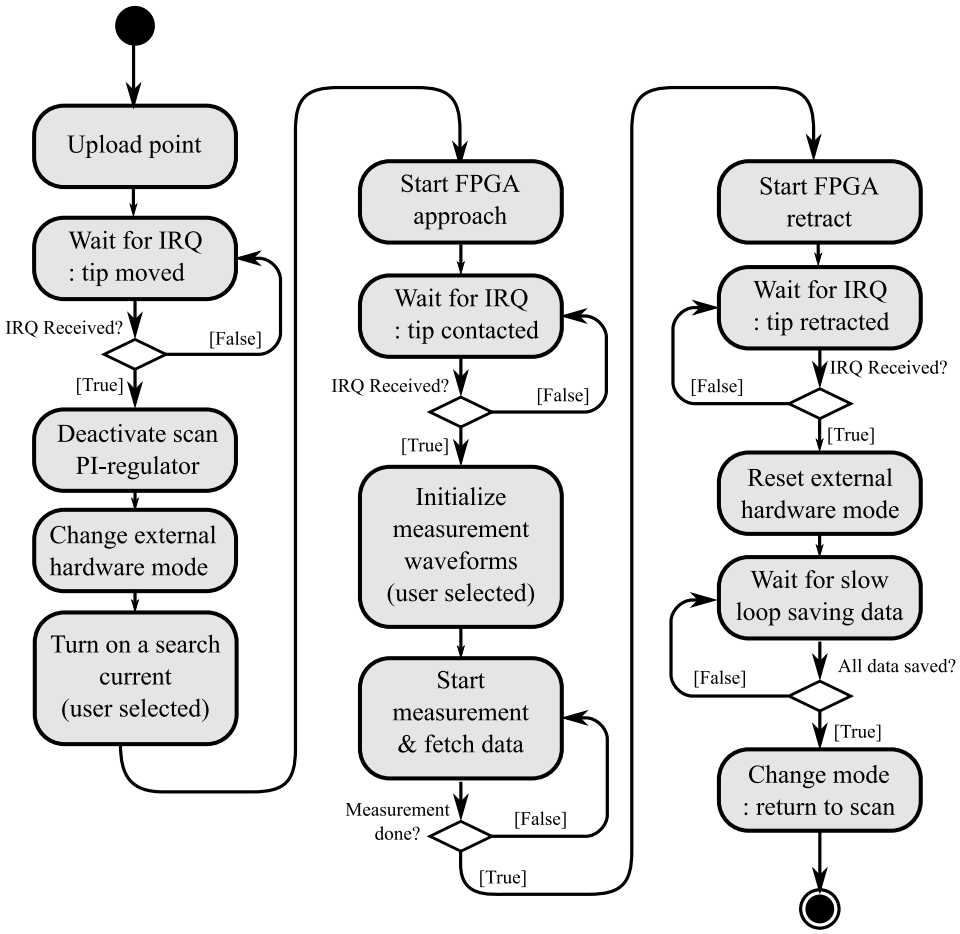

Figure 3.13: The point contact activity implemented as a state machine on the PXI host system.

loop is designed around a LabVIEW event handler structure, with user defined events like:

- **Scan frame restart.** Makes sure that all data of the current frame is saved to disc before a new frame can be started (see § 3.3.1). This is where the files corresponding to the scan frames are created and closed. At this point scan frame metadata is also saved to disc.
- **Initiate point contact measurement.** Start a new segment in the binary file for saving of the point contact measurement data with all the appropriate metadata.
- **Timeout event.** When no other events has happened, this code will take the responsibility of saving the incoming data to disc. If the "PCS Start" event was fired, this event will try to save incoming point contact measurement data; otherwise, scan data will be saved.

The timeout event is the major workhorse of the slow loop's code. The VI responsible for saving of scan data has to split the incoming data into two data streams: one for the "forwards" image, and one for the "backwards" image. The splitting is based on some "simple" bookkeeping; define

NP := # points per scanline

NF := # of points already saved to the "forwards" image

NB := # of points already saved to the "backwards" image

The splitting decision is made by (pseudo code):

```
#--------------------------------
if (NF % NP != 0) or (
( (NF % NP)==0 and (NB % NP)==0 )
and (NF/NP == NB/NP) ):
-- fill the forward line
else:
-- fill the backward line
#--------------------------------
```

where % is the modulus operation. This is repeated until all the data fetched from the RT FIFO has been saved to disc.

When saving point contact measurement data to disc, the code is more straight forward. The only concern is to take all the incoming data and save them disc. The data is placed in the file according to how much data that has been saved for the same measurement in previos iterations of the slow loop.

The slow loop contain code for streaming the scan data using TCP to a client computer. This is currently unused, as it has proved simpler to just plot the scan frames directly on the network published front panel of the PXI software.

3.3.2 Field Programmable Gate Array

The FPGA software and the FPGA's analog output channels (±10 V) are used for controlling all voltages applied to the piezoelectic tubes of the STM. The voltages designated for the piezo tubes are given from the FPGA's analog output channels, lying in the range ±10 V.

The FPGA features three main software control modes that are administered from a main software loop via *first-in-first-out* lists (FIFOs). The three control modes, are:

- Coarse Mode
- Scan Mode
- Point Contact Mode

.

Coarse Mode

The coarse approach software mode implements the tunneling contact searching algorithm described in § 3.1.3. This searching will be referred to as the "*auto approach*" sequence. The auto approach is implemented by ramping the voltage on the coarse-tube while monitoring the tunneling current's corresponding measured voltage at one of the analog inputs of the FPGA module. When a tunneling current is detected, a PI regulator is turned on, allowing the distance between the STM's tip and sample to remain constant, regardless of mechanical vibration, thermal expansion of the tubes, or similar effects. The differential term of the normal PID controller is left out due to its bad noise characteristics.

The output relating to the coarse mode's z-axis contraction and expansion has been split into two different outputs on the FPGA. The first is the base coarse mode voltage level and the other is the value from the coarse mode PI regulator. These two voltages are then summed using an external summing amplifier. The output from the summing amplifier is then fed through a gain-selectable high voltage amplifier that can give out voltages in excess of 200 V. Due to the piezoelectric cylinders having a depolarization threshold at around $V_{\text{depol.}} \simeq 150 - 200$ V, the maximum output is clamped to 100 V by the FPGA's software to prevent disaster. With the output voltages from the FPGA lying in the range ±10 V, this sets a limit of the external gain to $G_{\text{ext}} \leq 10$ V/V.

The PI regulator must be given enough leg- and headroom below and above its mean output level in order to ensure proper regulation without the voltages saturating or reaching otherwise dangerous levels. This is solved by only allow switching to the PI control on a measured tunneling contact if the coarse tube voltage is within a predetermined voltage subrange of the $0 - 100$ V range. With a maximum output voltage in the range ±100 V ($G_{\text{ext}} = 10$ V/V), this range is usually set to $V_{\text{allowed}} \in [+50, +80]$ V. This allows the PI regulator to add up to ±50 V on top of the coarse tube signal without the total voltage reaching negative values. For coarse tube voltages above 50 V the total voltage, (coarse

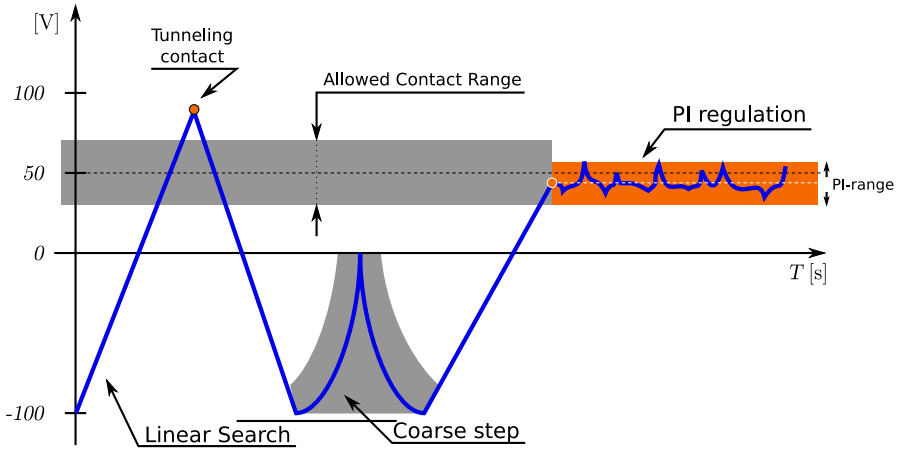

Figure 3.14: The coarse mode approach sequence, showing: the linear search with hit outside allowed searching region, a coarse step towards the surface, linear search with hit inside allowed region, and finally the PI regulator working to keep the tunneling current constant.

tube+PI) will be clamped. If something fails, the output on the coarse tube can be brought to 0 V, either by a failsafe software function or by manually turning of the high voltage amplifier.

If the requested tunneling current is found within the upper range of the incremental voltage ramp, the output voltage is brought to zero and a coarse step is performed, throwing the tip a small step closer to the sample. A new incremental search is started, now with the tip starting a bit closer to the sample surface than in the previous try. This way the regulation can be started in the correct range.

The coarse step inertial slider mechanism introduced in § 3.1.3 is implemented by a swift half-cycloid exitation waveform, giving a rapid acceleration of the tip, followed by a downstep in the output voltage[29]. The result of such a waveform is that the tip is "thrown" loose from the containing glass cylinder, moving it a small distance within the tube. This distance has been previously measured to $50 - 500$ nm depending on the cycloid's amplitude and the tip's static friction to the inner quartz tube (cf. § 3.1). This is smaller than the full static range of the piezotube with 100 V applied over its electrodes, given by the piezoelectic tubes' voltage–displacement properties (see Eq. (3.1.2)).

The coarse mode also has a few extra features that allows manual adjustments of the tip. These are:

- **Single steps**: a single step can be used to force a coarse step during auto approach. This is useful whenever the auto approach locks on a false or otherwise noisy transient. Single steps can be done in both directions.

- **Manual approach & retract**: manual approach and retract are just contiuous series of coarse steps in either direction. These modes are mostly

used when inserting a new tip and tipholder into the STM. By simply inserting the tip holder (with the tip) a few millimetres into the glass tube and using the manual retract function to pull it into the glass tube, it is easy and safe to change tips. If the tip is brough all the way into the glass tube before the sample holder is inserted into the STM's tower head, there is no real chance that the tip will be "crashed" by accident.

Scan Mode

The scan mode is implemented as a loop where the tip is moved in straight lines in the x- and y-planes using linear interpolation between selected points while a PI regulator is running on the outer piezoelectric tube. During the scan, the PI regulator that ran on the inner piezo tube during coarse auto approach is turned off, and the voltage on the inner tube is kept constant. Scan mode allows the use of a smaller gain than that required for auto approach, consequently providing higher vertical resolution than possible with the coarse tube alone.

The control points are uploaded from the host system, ie. the system containing the FPGA module (described later in the text), via a 32 bit high speed direct memory access (DMA) channel. The x- and y-coordinates are calculated as 16 bit signed integers on the host system, then packed to a 32 bit number with the x coordinates as the most signifant bits and the y coordinates as the least significant bits, before they are transfered on the DMA channel to the FPGA.

On the FPGA, the vector of points received on the DMA channel is extended in size by linear interpolation to intermediate values of the uploaded coordinates. The tip is moved through the expanded list of points. The factor of expansion is set by several factors, including scan range, scan speed, PXI and FPGA loop rates, and piezo constants. For an atomic resolution image at 4 by 4 nm at 256 points by 256 scanlines, a speed of 4 nm/s with loop rates 1000 μs and 5 μs for the PXI and FPGA respectively, the total expansion will be in the order of 1000 points.

This extension of the number of points ensures a higher noise immunity, as averages of the applied z-axis voltage,V_z, and the measured tunneling current, I_t, are calculated for all the intermediate points, before they are transfered back to the PXI system. The usual way of running the scan mode involves uploading a list of coordinates corresponding to a scanline. A simple method used to estimate the quality of an STM image is to sweep the tip in both directions, recording a forward sweep as well as a backward sweep image. These duplicate images should ideally be identical, but in reality, they never are. This is due piezoelectric "creep", thermal expansion and noise.

As all transitions between scan points occur by interpolation of intermediate points, the scan mode can be used for safe positioning of the tip to an arbitrary coordinate if the measured values to and from this point is not uploaded to the host PXI system. This feature is used in combination with the point contact software mode described in the following section.

Point Contact Mode

The last mode on the FPGA allows the tip to indented into the sample, effectively making a point contact. The point contact mode is initiated from the scan mode. This is controlled by the user via the PXI host system software:

1. The scan mode positions the tip to a user defined coordinate.

2. The PXI software is notified by an IRQ that the tip is in position and ready for point contact approach.

3. The host and the FPGA change their software modes to the point contact mode.

4. When appropriate conditions for indentation are met, the FPGA triggers a second IRQ telling the PXI system to initiate measurement.

5. When the measurement is completed, the PXI system tells the FPGA to retract the tip, before the modes are again switched back to the scan mode.

There are basicly two ways of making a user defined point contact:

1. Define a desired indentation depth through a voltage limit on the piezo tube. As the tip–sample separation distance is known from the measured tunneling current via the tunneling relations (see § 2.1.1), one may set a voltage limit on the piezo corresponding to a specific indentation depth.

2. Define a desired contact resistance. The tip can be lowered while applying a current through the junction. If the tip–sample junction resistance is measured while approaching, it is possible to stop the approach when reaching a predetermined resistance. This is related to the point contact cross sectional area via the Sharvin resistance, assuming a ballistic contact (see Eq. (2.1.17)). This further allows a user defined current density, which is particularly useful for investigating spin transfort effects.

Both approaches have their advantages. Number 1 has the advantage that it is easy to implement and can be performed with only one measurement of the tunneling current. Number 2 can give more control over the point contact's characteristics, but is harder to perform as it requires two measurements; of both the current through and the voltage drop over the junction, as well as a calculation of the contact resistance. The second approach also relies on the use of a very stable current or voltage source.

In our system we focus on the second method. By switching the hardware mode of the splitter board to the point contact mode before approach, a "search" current may be applied through the tunneling junction during approach. In addition, the voltages across the tunneling junction and the measurement resistor (low side measurement shunt) (see Figure 3.5) are measured on two analog inputs on the FPGA, allowing us to monitor the resistance in the point contact during approach.

The voltage drop across the measuring shunt is given by:

$$V_{\text{meas}} = I_{\text{search}} R_{\text{meas}} \ , \tag{3.3.3}$$

where the measurement resistor has been predetermined to $R_{\text{meas}} = 51.5\ \Omega$ and $I_{\text{search}} \simeq 1 - 1000\ \mu$A is the searching current The ideal value seen on the FPGA in signed 16 bit integer representation on the FPGA is:

$$V_{\text{meas}}^{\text{FPGA}} = \frac{(2^{15} - 1) V_{\text{meas}}}{V_R} \ , \tag{3.3.4}$$

where $V_R = 10$ V is the maximum amplitude on the FPGA analog inputs.

The sum of the user selected contact resistance, R_s and R_{meas} multiplied by I_{search} must not exceed the maximum output voltage swing on the current sender (~ 12 V), see § 3.2.2). The ideally measured voltage, V_j^{FPGA}, over the contact junction as seen on the FPGA is given by:

$$V_j^{\text{FPGA}} = \frac{(2^{15} - 1) R_s I_{\text{search}}}{V_R} \ . \tag{3.3.5}$$

The applied voltage over the contact junction will remain saturated ($\simeq 12$ V) until the combined resistance of the measurement shunt and the contact junction drops below the resistance given in Eq. (3.2.2). When the measured current has reached the search current, the tip is indented further into the sample until the measured voltage across the contact junction drops below V_j^{FPGA}. Assuming neglible noise, the point the contact resistance will be guaranteed to be smaller than R_s.

When a contact of the selected resistance has been achieved, any measurement involving arbitrary user selected current, voltages or magnetic field waveforms can be performed. The different measurement waveforms will be treated later in this chapter. When a point contact measurement is completed, the FPGA is put into a retract phase (still in the coarse mode), pulling the tip the same number of steps back from the sample as the approach phase indented it. After the tip has been retracted, the FPGA is switched back to scan mode, turning on the PI regulator, allowing the scan to continue where it left of.

3.4 Samples

Sputtered metallic multilayer samples was created by Qiu Xuepeng, Shiming Zhou group, at the Fudan University, Shanghai, China. The sample studied in this thesis is a magnetic spin valve structure, having the composition Ta(3 nm)/FeMn(8 nm)/FeNi(8 nm)/Cu(3 nm)/FeNi(3 nm)/Cu(10 nm)/Si. Here Si is the substrate, FeNi is the ferromagnet ($T_C \simeq 600$ K); FeMn is the antiferromagnet ($T_N \simeq 450$ K) used for pinning the topmost FeNi layer via the exchange bias effect; Cu is used as the paramagnetic metallic spacer material; while Ta is the metallic capping layer. The FeMn/FeNi interface is exchange biased with a measured calibration exchange field of $H_E \simeq 200$ Oe.

Chapter 4

Results and Discussion

4.1 Giant Magnetoresistance

Giant Magnetoresistance (GMR) was measured in the spin valve sample system at room temperature and atmospheric pressure. A point contact was made, a current of a few mA was turned on, and the external field was swept to flip the orientation of the free layer. Figure 4.1 shows a typical measured GMR curve. The onset of the first GMR top is caused by reversal of the free layer; the first drop is caused by the reversal of the pinned FM layer, as the exchange bias field is overcomed; the second top is the repinning of the exchange biased layer; while the second drop is the free layer again coupling ferromagnetic to the (re)pinned layer.

Figure 4.2 shows a larger part of the measurement data used to generate Figure 4.1. The point contact was maintained for several seconds while the field was swept with a 4 Hz positive offset triangular wave. As the base resistance changes only slightly for the full five seconds, Figure 4.2 illustrates the excellent stability of the point contacts attainable with the STM.

4.2 Spin Transfer Torques

Wei et al. [37] reported on a changing exchange bias in spin valves as a function of applied current. The samples studied was similar to the one used in our measurements, except subtle differences in layer thicknesses, and the fact they used CoFe instead of FeNi for the ferromagnetic layers. One major difference is is that Wei et al. used a thick (50 to 100 nm) underlayer of Cu to secure a closely perpendicular-to-plane flow of the current, across the spin valve, and into the Cu buffer. This is in stark contrast to our sample which only has a 10 nm underlayer of Cu.

To compare with the results of Wei et al., field sweeps at different levels of constant current through the point contact was performed. The changing exchange bias can be visualized by plotting the GMR curves in a current–field contour plot, with the normalized resistance ($R^* \in [-1, 1]$) as the color of the

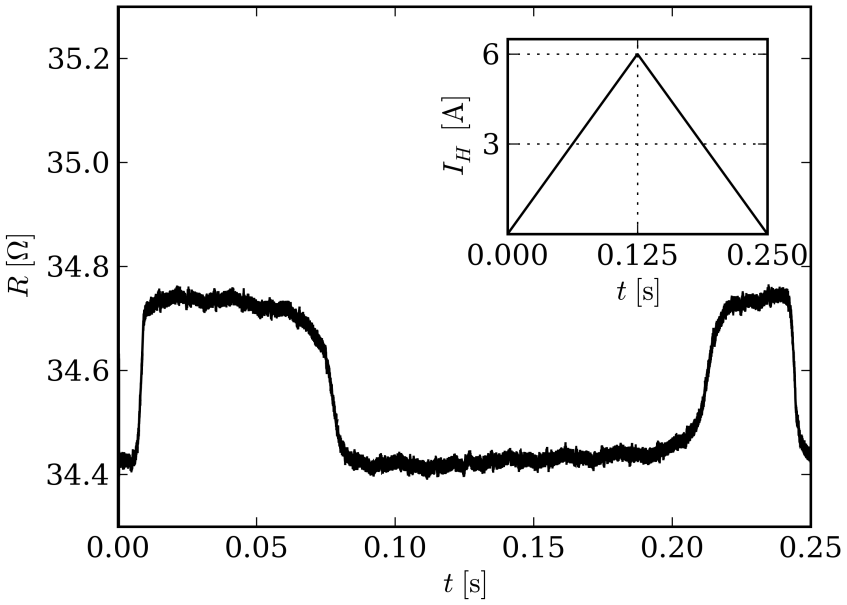

Figure 4.1: Point contact measurement showing a 1% relative change in the resistance due to the GMR effect. A current of $I = 10\text{mA}$ was sent through the sample while the magnetic field was swept with a triangular wave (see inset).

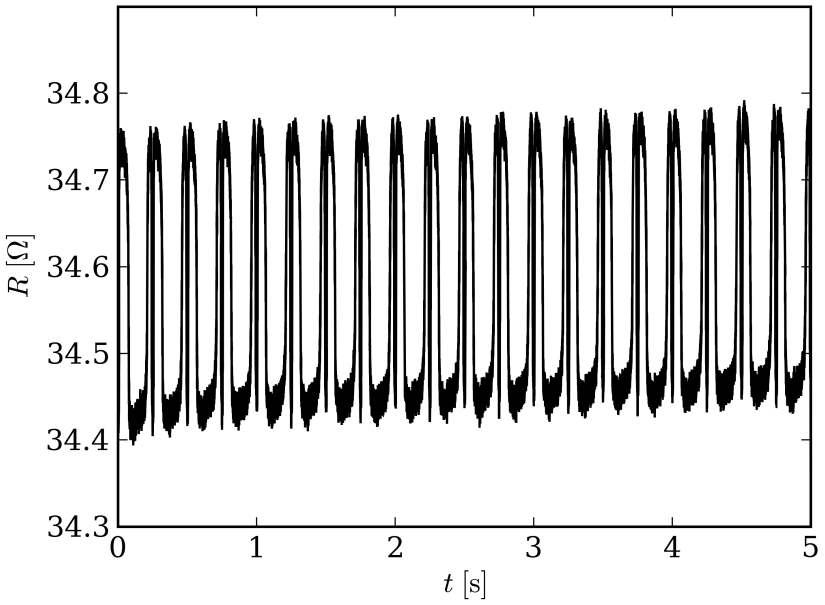

Figure 4.2: Point contact measurement showing several successive GMR curves, generated by sweeping the 4 Hz external field while keeping the current through the contact at a constant level.

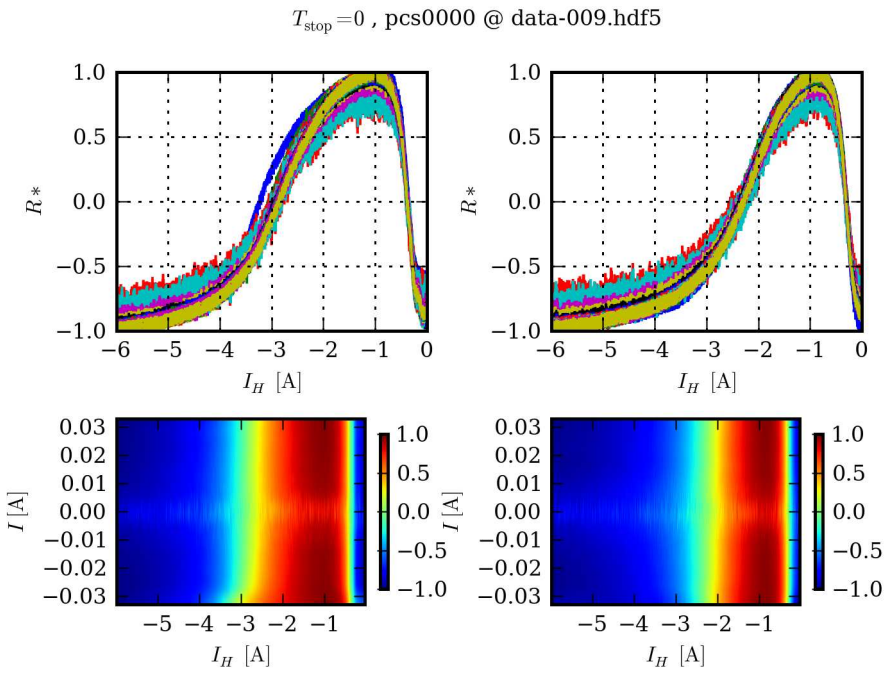

Figure 4.3: Resulting normalized GMR curves after the magnetic field was swept using a 4 Hz triangular wave, and the current was varied in steps from −33 mA to +33 mA. The upper left shows the GMR step from the magnetic field increase, while the upper right shown the GMR step from the magnetic field decrease. The lower row of contourplots correspond to the measurements in the first row, now with the normalized resistance as the color.

plot (see Figure 4.3).

A change in the exchange field independent on the direction the current was changed was observed. This is in contrast to the measurements performed by Wei et al., and can as such not be explained by spin transfer torques acting on the local AFM domains. The cause of the effect is related to the training effect (cf. § 2.2) and will be treated in the next section.

No ordinary spin transfer switching have been observed on the spin valve's free layer. This can be explained by considering the structure of the thin film sample. As mentioned above, the thin film has a rather thin base Cu layer beneath the free layer and on top of the Si substrate. As the Si substrate is not conducting, the electrical contact between the sample and sample holder is mediated by a CuBe retention flap that is in contact with the sample's top surface. Since the two FM films are ferromagnetically coupled, as illustrated by the free layer exchange field offset in the GMR curves (cf. Figure 4.1), only electrons reflecting from the pinned FM layer can make the free layer's magnetization switch or make it start precessing (cf. § 2.5.2). As all the sample's layers are metallic with comparable conductivities, the current will spread within the layers, making it almost impossible to achieve the required ballistic perpendicular-to-plane (CPP)

positive current density required to get current induced switching of the free layer.

4.3 Training and Recovery of Exchange Bias

The field–current–resistance plots of the previous section had a slant in the exchange field strength which proved to be independent of the stepping direction and magnitude of the current used. Because of this, similar measurements with field sweeps under *constant* current was performed. The current was kept constant while sweeping the magnetic field with triangular waves for a period T_{on}, after which the field was turned off for T_{stop} seconds, before the field waveform was turned back on for some periods of the field cycle (see Figure 4.4 for an example coil exitation waveform).

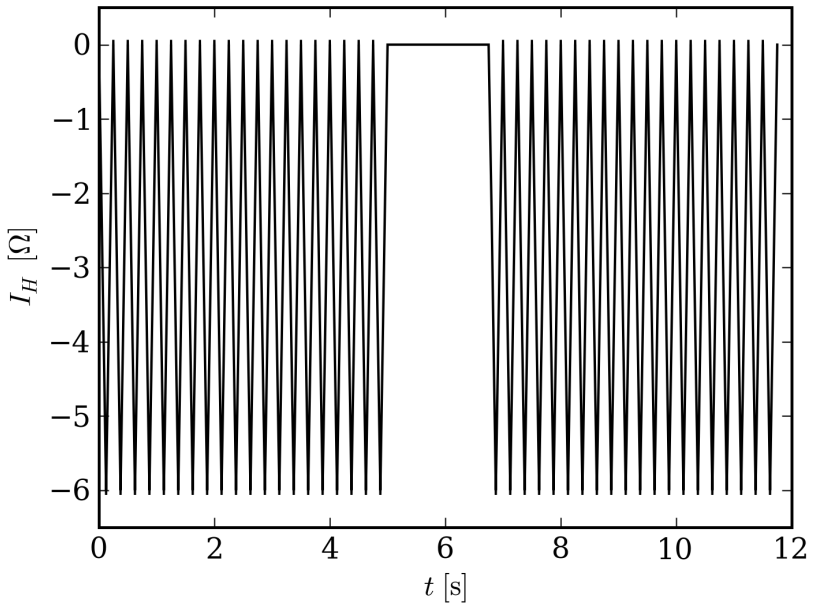

Figure 4.4: Example exitation waveform for the electromagnet's coils. A triangular coil current with output swing $|A| = 6$ A and frequency $f4$ Hz is used to "train" the exchange bias for $T_{\text{on}} = 5$ s before the field is turned off for the stop period T_{stop}. The field is then turned back on for several seconds.

Measurement series with the stop time T_{stop} as the main parameter was captured. Figures 4.5, 4.6, 4.7, 4.8, 4.9 and 4.10 show selected measurements from a series with $f_{\text{magnet}} = 4$ Hz, $T_{\text{on}} = 6.8$ s and varying T_{stop}. The current was kept at a constant at $I = 10$ mA for each measurement. In each of the figures, the top right shows the reversal of the pinned layer (shown in blue) taken at the $R^* = 0.0$ crossings of the normalized resistance for GMR tops in the field increase interval of the field sweep. The green curves are the $R^* = 0$ crossings of the corresponding repinning fields. The exchange field is then defined as the

mean of the blue and green curves, thus lying halfway between them.

The stop interval, $t \in [T_{\text{on}}, T_{\text{on}} + T_{\text{stop}}]$ s, is marked by a gray bar spanning the vertical range. As can be seen from the figures, the exchange field changes swiftly when starting out the measurement before it falls off at slower steady rate. This is expected from the exponential dependence of the exchange bias in a reverse magnetic field (cf. Eq. (2.2.1) and Xi et al. [41, 40]). The figures show that when the field sweeps are started up again after the stop interval, the exchange field has "recovered". Thus, a stronger field is required to switch the pinned layer than what was needed in the last period before the stop interval. Comparing the different figures, a longer stop interval, T_{stop}, results in a stronger recovery of the exchange bias. As the junction current was kept constant during the stop period, the effect is not caused by joule heating. It can be attributed to the complex recovery of the AFM domains from the training effect[10, 25].

By defining the exchange bias recovery as:

$$\Delta = \left|\frac{I_H^{\text{r}} - I_H^{\text{s}}}{I_H^{\text{s}} - I_H^{\text{u}}}\right| , \tag{4.3.1}$$

where I_H^{u} is the exchange field for the very first GMR sweep, I_H^{s} is the exchange field for the last GMR sweep before the field sweep is stopped, and I_H^{r} is the exchange field just after recovery. With this definition, each of the point contact measurements within one series will generate one datapoint for the relation $\Delta = \Delta(t_{\text{stop}})$. Figure 4.11 shows the measured recovery as a function of the logarithm of the stop time, t_{stop}, for three different measurement series where the main parameter variation were to the on-time, T_{on}, and with slight changes to the magnetic field sweep frequency, f_{magnet}. Linear regression on the three series, give:

$$\Delta_0 \approx 11.5346 \ln(\nu_0 t_{\text{stop}}) + 53.5146 , \quad e_2 = 1.74816 \tag{4.3.2}$$

$$\Delta_1 \approx 13.0958 \ln(\nu_0 t_{\text{stop}}) + 53.5547 , \quad e_0 = 2.84315 \tag{4.3.3}$$

$$\Delta_2 \approx 14.0940 \ln(\nu_0 t_{\text{stop}}) + 38.6173 , \quad e_1 = 3.53877 \tag{4.3.4}$$

$$\tag{4.3.5}$$

where $[\nu_0] = \text{s}^{-1}$ is a characteristic frequency, assumed to be unity for convenience; and e_i is the mean square error of the regression. As the curves with similar on-time are markedly shifted from the third one (see Figure 4.11), one may assume that the constant regression coefficient b (from the relation $\Delta = a \ln(\nu_0 t_{\text{stop}}) + b$) will depend on the total training time, T_{on}, or the number of cycles of the field[1], and on the field frequency, f_{magnet}. As three curves are not enough to find the dependency of these two parameters, yet alone one parameter, the data collected this far is inconclusive in regards to the dependencies of a and b. Yet, an extrapolation to find the total needed time for full recovery of the exchange bias can be attempted. Defining it as:

$$\begin{aligned} t_{\text{stop}-\text{total}} &= t_{\text{stop}}(\delta = 100) - t_{\text{stop}}(\delta = 0) \\ &= \frac{1}{\nu_0}\left[\exp\left(\frac{100 - b}{a}\right) - \exp\left(\frac{-b}{a}\right]\right) . \end{aligned} \tag{4.3.6}$$

[1] closely related to the total training time

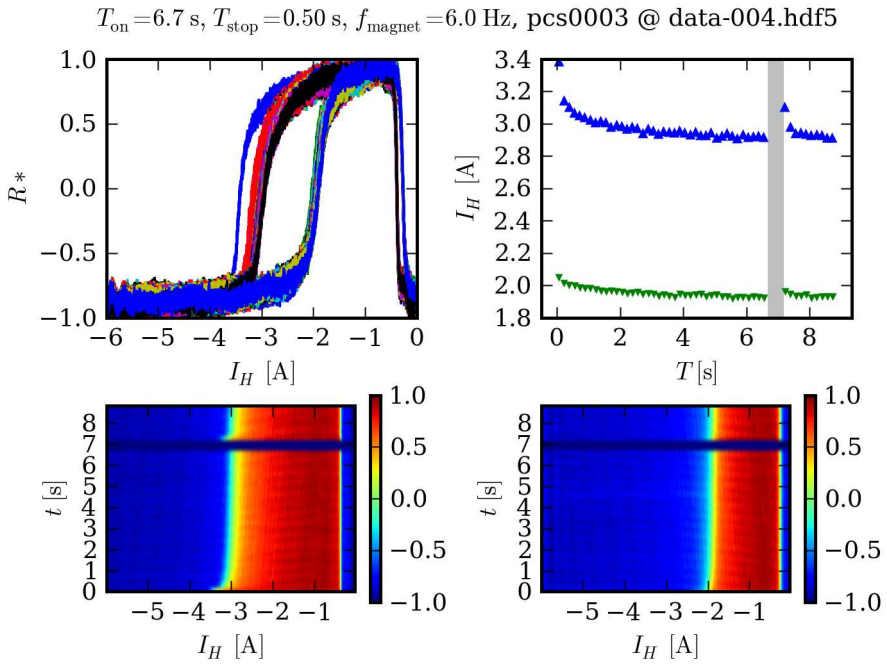

Figure 4.5: GMR series measurement where the magnetic field was turned off after T_{on} seconds for a duration of T_{stop} seconds.

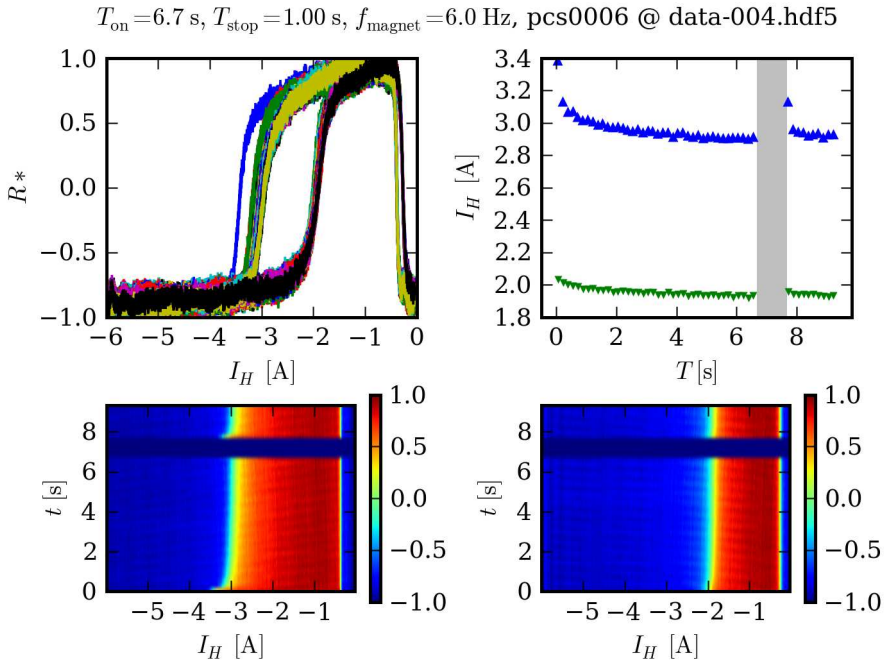

Figure 4.6: GMR series measurement where the magnetic field was turned off after T_{on} seconds for a duration of T_{stop} seconds.

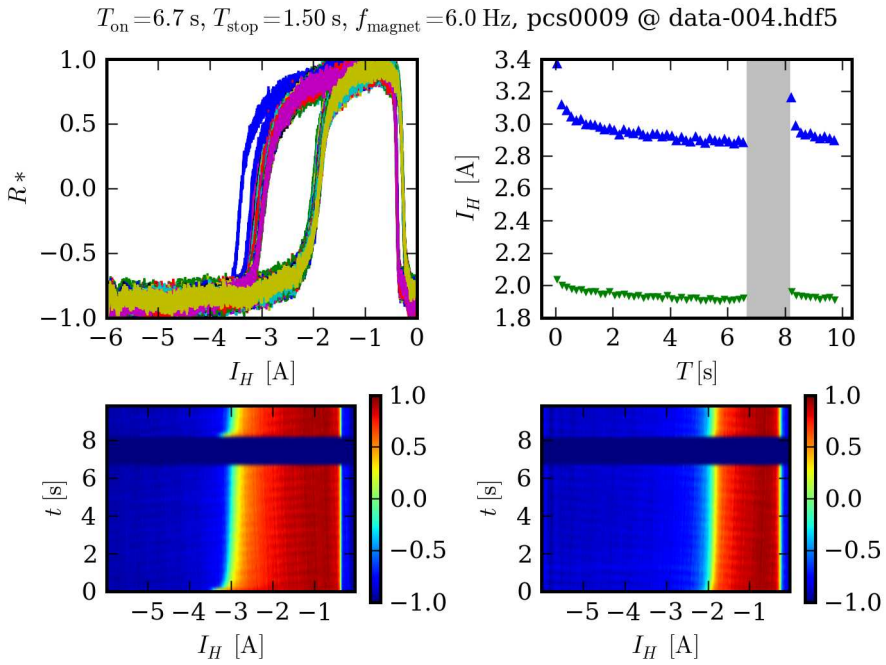

Figure 4.7: GMR series measurement where the magnetic field was turned off after T_{on} seconds for a duration of T_{stop} seconds.

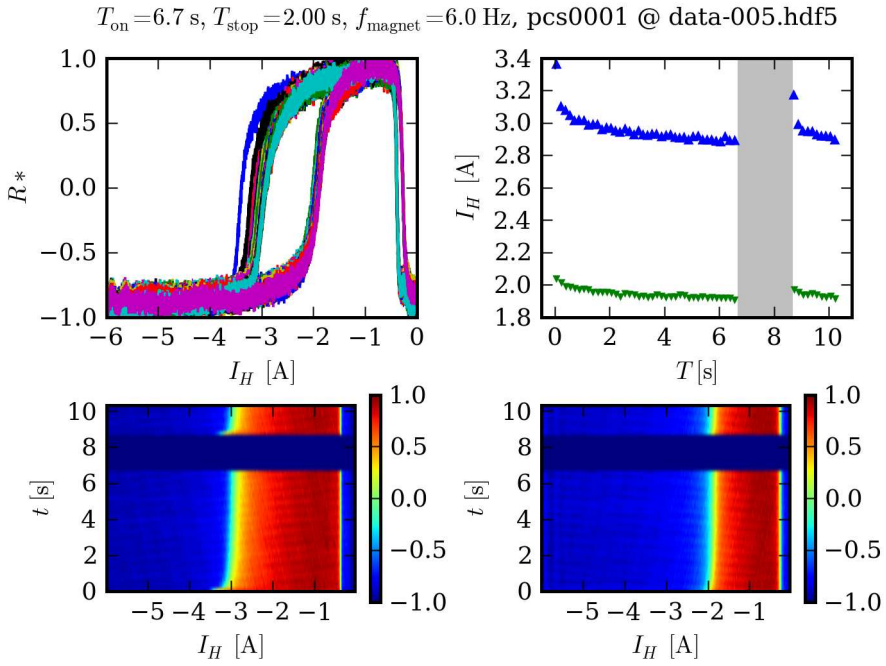

Figure 4.8: GMR series measurement where the magnetic field was turned off after T_{on} seconds for a duration of T_{stop} seconds.

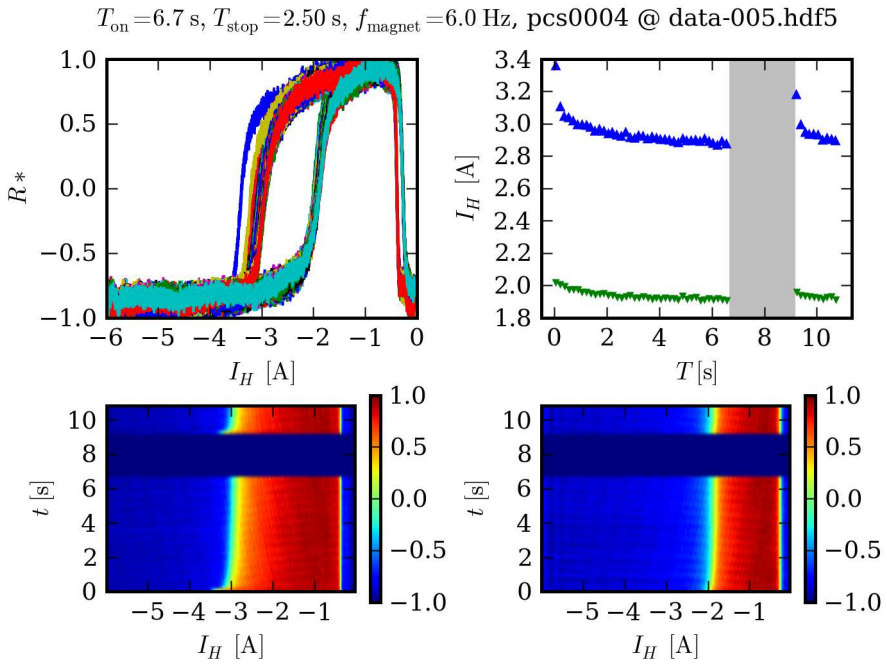

Figure 4.9: GMR series measurement where the magnetic field was turned off after T_{on} seconds for a duration of T_{stop} seconds.

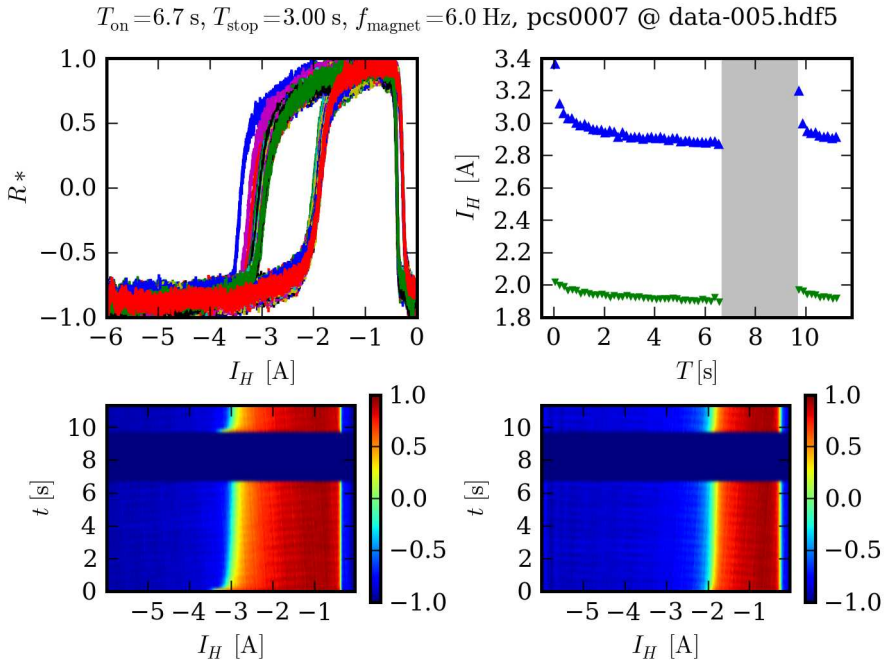

Figure 4.10: GMR series measurement where the magnetic field was turned off after T_{on} seconds for a duration of T_{stop} seconds.

This gives total recovery times of: $t^{(0)}_{\text{stop-total}} \approx 56.3s$, $t^{(1)}_{\text{stop-total}} \approx 34.7s$, and $t^{(2)}_{\text{stop-total}} \approx 77.8s$. With such a large spread, more measurements are needed to be able to explain the large deviations. Nevertheless, the recovery has been shown to depend logarithmically on the stop time.

If a recovery of 100% is defined as the original direction of the AFM/FM exchange field, then 0% recovery amounts to a completely reversed magnetization. As such, the total magnetization of the AFM/FM bilayer structure will have the same $\ln(\nu_0 t)$ dependency as the recovery[25]. This is in agreement with Dho et al. [10] and Pina et al.[25]. Dho et al. fitted exchange field data to a similar logarithmic dependency as the one seen here. They proposed a model based on the idea of thermally activated relaxation of the AFM's domains. With their model, the relaxation can be treated much in the same way as isothermal annealing in amorphous metals. The measurements of Dho et al. were on time scale 1–2 orders of magnitude larger than in our measurements.

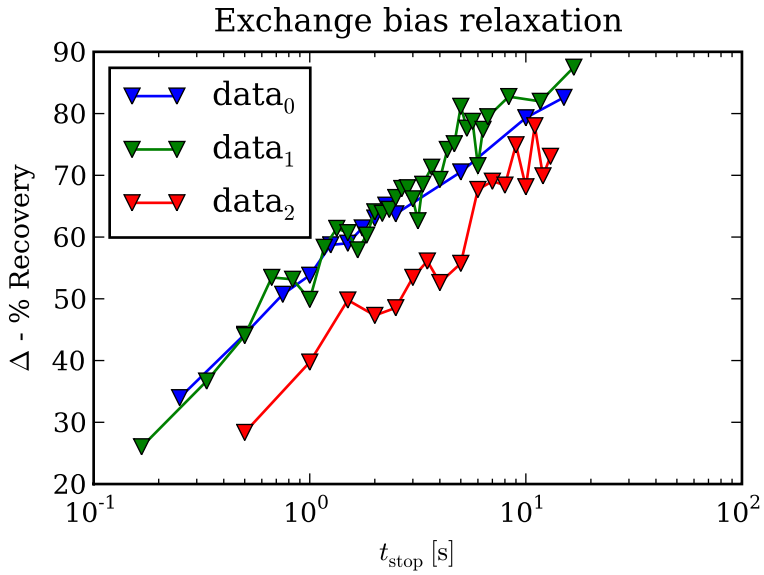

Figure 4.11: Exchange bias recovery as a function of relaxation time. The curves are parametrized by: $\text{data}_0(f_{\text{magnet}} = 4$ Hz, $T_{\text{on}} = 5$ s); $\text{data}_1(f_{\text{magnet}} = 3$ Hz, $T_{\text{on}} = 6.7$ s); and $\text{data}_2(f_{\text{magnet}} = 2$ Hz, $T_{\text{on}} = 20$ s)

Chapter 5

Conclusion

The STM

The in-house built STM system has reached a functional stage in its development, where it has become feasible to start using it for real measurements. This has been demonstrated by the measurements presented in Chapter 4, both by the stability of the point contacts with large junction currents; the general noise levels, being 40-60% lower than before; and the excellent timing seen in the exitation waveforms and measurements and the consistency observed between different measurement series.

The current behaviour of the software is at a stage where the measurement data is saved in a consistent state, the overall system generally does what it is supposed to and *most* of the major show-stopper bugs in the PXI and FPGA's software have been corrected.

Measurements

Giant magnetoresistance, $\Delta R \sim 1\%$, have been observed in a metallic spin valve structure (FeMn(8 nm)/FeNi(8 nm)/Cu(3 nm)/FeNi(3 nm)). The point contacts made with the STM are stable at a time scale of several seconds, making repeated GMR measurements possible.

Exchange bias training effects have been observed in the spin valve structure by repeated cycling of an external magnetic field, with an amplitude large enough to overcome the exchange bias of the AFM/FM interface. The measurements was performed with constant current through the contact junction, clearly indicating that the effect can not be attributed to joule heating. The second reversal, or relaxation, of the exchange field has been observed to obey a logarithmic time dependency, consistent with measurement results obtained by Dho et al. [10]. The logarithmic time dependence results in a total recovery time in the order of ~ 50 s.

5.1 Further Work

Several areas need attention for the goals of the STM to be fulfilled. Suggested improvements include:

- Separation of the tunneling- and the point contact signal lines on the splitter board. This should provide less noise in both cases, as fewer active components will be attached to the system when measuring. By separating the point contact signal line, a better matched instrumentation amplifier can be chosen.
- Doing more of the speed critical handling of large data arrays in C (using LabWindows/CVI). This can be used to avoid copying of large data arrays, which happen at unwanted places automatically in LabVIEW.
- Dispite the working state of the software's functionality, there are certain shortcommings in the software design that makes it hard to modify the code and correct those problems that occur. This include the complexity of the current LabVIEW code, which makes debugging an almost impossible process. Revising the general structure, combined with the previous mentioned point should provide a better system.
- Streaming waveform segments from the PXI system to the multifunction DAQ as the measurements progresses. This must be implemented in order to do measurements on a longer timescale at full resolution and sampling frequency, as not to max out the memory of the multifunction DAQ upon initialization.
- Ensure better signal resolution during point contact approach. This is to improve the resistance selection.

Appendix A

Measurement File Format

A.1 Hierarchical Data Format

The measurement files are saved with the *Hierarchical Data Format version 5* (HDF5) file format in files called data-xxx.hdf5. The HDF file format is open source, and is thus provided without charge by the HDF Group[15]. It is a completely portable format, with built in handling of platform specific featuress like endianness. HDF5 files are comprised of groups, datasets and attributes. The groups act as containers for the datasets, while the attributes are used for attaching metadata to both groups and datasets. The datasets are objects composed of collections of data elements or raw data. Combined with the metadata, in the form of attributes, the datasets can be made to contain all data necessary to write, read and interpret the stored data. A dataset is comprised of a dataspace and a datatype. Examples of datatypes can be floating point numbers, signed or unsigned integers, characters and many, many more (see Table A.1 for an overview). Like in most programming languages, user defined types can be built up from the types provided by the HDF5 library. The dataspaces defines how the data in a dataspace is ordered. A dataspace can be of scalar size, multidimensional arrays with predetermined sizes, or unlimited arrays of arbitrary dimensions.

A.2 Format Specification

A folder for the current date is created in the base folder selected on the PXI front panel. The date folder is given the name "yy-mm-dd", where yy is the year, mm is the month, and dd is the day. One file is created for each scan frame, and the file is saved in the correct date-folder as: data-00x.hdf5. The scandata can be found in the datasets "/scan/forward" and "/scan/backward" as a $[4, \text{size}(0) \cdot \text{size}(1)]$ sized 2-dimensional array of H5T_STD_I16BE integers. The scanframe attributes, listed in Table A.2, are saved in the group "/scan" and not in the datasets, as the two datasets share the same attributes.

Point contact data are saved in the group "/pcs" in datasets called "pcsX",

Type Specifier	Description
H5T_IEEE_F32BE	Four-byte, big-endian, IEEE-floating point
H5T_IEEE_F32LE	Four-byte, little-endian, IEEE-floating point
H5T_IEEE_F64BE	Eigth-byte, big-endian, IEEE-floating point
H5T_STD_I32BE	Four-byte, big-endian, signed two's complement integer
H5T_STD_U16LE	Two-byte, little-endian, unsigned integer

Table A.1: Examples of typical data types provided by the HDF5 library.

Name	Type Specifier	Description
size	(2x) H5T_STD_I16BE	
dimensions	(2x) H5T_IEEE_F32BE	Scan frame size in nm
scan_speed	(2x) H5T_IEEE_F32BE	Scan speed in nm/s
alfa_x_min	H5T_STD_I16BE	
offset	(2x) H5T_IEEE_F32BE	Scan frame offset in nm
comment	H5T_STRING	Description of image
current_setpoint	H5T_IEEE_F32BE	Regulation setpoint in nA
bias_voltage	H5T_IEEE_F32BE	Tip–sample bias voltage
PIDs	(3x) H5T_STD_I16BE	Scan regulator coefficients
PID_range	(2x) H5T_STD_I16BE	Output ranges within ±10 V in 16 bit format
gain_PIDs	H5T_IEEE_F32BE	Scan PID signal'- external gain
gain_XY	H5T_IEEE_F32BE	XY signal'- external gain

Table A.2: Scan frame attributes. These reside in the "/scan" group.

where the X is a four field zero padded integer starting from 0 for each scan frame. Each point contact dataset has a large number of attributes, listed in Table A.3. The dataset contains a 2-dimensional array of data, where the first column is the measured voltage over the contact junction and the second column is the measured voltage over the, currently, 51.5 Ω low side measuring shunt. The exitation waveforms can be rebuilt from the tip_current_wfm and magnet_wfm attributes of the dataset. These are arrays of compound datatypes, for each segment with time duration $T_{\text{seg}} = \frac{L_{\text{attr.}}}{\text{duration}}$, where $L_{\text{attr.}}$ is the length of the attribute array. The compound datatype consists of: an enumeration telling what kind of waveform each segment is (sine wave, square wave, triangular wave or sawtooth), the amplitude, the frequency, the offset and the phase of the segment.

Name	Type Specifier	Comment
gain_PCSz	H5T_IEEE_F32BE	
samplingrate	H5T_IEEE_F32BE	
duration	H5T_IEEE_F32BE	
resistance_contact_limit	H5T_IEEE_F32BE	
AOZ_limit	H5T_IEEE_F32BE	
coordinate	(2x) H5T_STD_I16BE	within scanframe
offset	(2x) H5T_IEEE_F64BE	column offset in V
Gain	(2x) H5T_IEEE_F64BE	column gain in V/V
magnet_wfm	H5T_COMPOUND	coil exitation parameters
tip_current_wfm	H5T_COMPOUND	tip exitation parameters
Resolution	H5T_STD_I32BE	# bits of resolution
search_current	H5T_IEEE_F32BE	used for approach
voltage_gain	H5T_IEEE_F32BE	external gain V/V

Table A.3: Point contact measurement attributes. These reside in the "/pcs/pcsXXXX" datasets.

Bibliography

[1] M. N. Baibich, J. M. Broto, A. Fert, F. Nguyen Van Dau, and F. Petroff. Giant magnetoresistance of (001)Fe/(001)Cr magnetic superlattices. *Phys. Rev.*, 61(21):2472–2475, 1988.

[2] J. Bardeen. Tunneling from a many-particle point of view. *Phys. Rev.*, 6(2):57–59, 1961.

[3] L. Bergen. Emission of spin waves by a magnetic multilayer traversed by a current. *Phys. Rev. B*, 54(13):9353–9358, 1996.

[4] L. Berger. Multilayers as spin-wave emitting diodes. *J. Appl. Phys.*, 81(8):4880–4882, 1997.

[5] A. E. Berkowitz and Kentaro Takano. Exchange anisotropy - a review. *J. Magn. Magn. Mater.*, 200:552–570, 1999.

[6] G. Binasch, P. Grünberg, F. Saurenbach, and W. Zinn. Enhanced magnetoresistance in layered magnetic structures with antiferromagnetic interlayer exchange. *Phys. Rev. B*, 39(7):4828–4830, 1989.

[7] G. Binnig and H. Rohrer. 7x7 reconstruction on si(111) resolved in real space. *Physical Review Letters*, 50(2):120–123, 1983.

[8] G. Binnig and H. Rohrer. Scanning tunneling microscopy. *Surface Science*, 126:236–244, 1983.

[9] G. Binnig, H. Rohrer, Ch. Gerber, and E. Weibel. Tunneling through a controllable vacuum gap. *Applied Physics Letters*, 40(2):178–180, 1982.

[10] Joonghoe Dho, C. W. Leung, and M. G. Blamire. Universal time relaxation behaviour of the exchange bias in ferromagnetic/antiferromagnetic bilayers. *J. Appl. Phys.*, 99:033910–5, 2006.

[11] A. M. Duif, A. G. M. Jansen, and P. Wyder. Point-contact spectroscopy. *J. Phys.: Condens . Matter.*, 1:3157–3189, 1989.

[12] I. Ekvall, E. Wahlström, D. Claesson, H. Olin, and E. Olsson. Preparation and characterization of electrochemically etched W tips for stm. *Meas. Sci. Technol.*, 10:11–18, 1999.

[13] R.M. Feenstra, J.A. Stroscio, and A.P. Fein. Tunneling spectroscopy of the Si(111)2x1 surface. *Surface Science*, 181:295–306, 1987.

[14] T. L. Gilbert. *Phys. Rev.*, 100:1243, 1955.

[15] The HDF group. `http://www.hdfgroup.org`.

[16] P. M. Haney and A. H. MacDonald. Current-Induced Torques due to Compensated Antiferromagnets. *Phys. Rev.*, 100(19):196801(4), 2008.

[17] P.C Hemmer. *Kvantemekanikk*. tapir akademisk forlag, 5 edition, 2005.

[18] A. G. M. Jansen, A. P. van Gelder, and P. Wyder. Point-contact spectroscopy in metals. *J. Phys.: Solid St. Phys.*, 13:6073–6118, 1980.

[19] L.D. Landau and E.M. Lifshitz. *Phys. Zs. Sowjet.*, 8(153), 1935.

[20] Sadamichi Maekawa. *Concept in Spin Electronics*. Oxford Science Publications, 2005.

[21] J. C. Maxwell. *A treatise on electricity and magnetism*. Clarendon Oxford, 1904.

[22] W. H. Meiklejohn and C. P. Bean. New Magnetic Anisotropy. *Phys. Rev.*, 102(5):1413–1414, 1956.

[23] J. Nogués and Ivan K. Schuller. Exchange bias. *J. Magn. Magn. Mater.*, 192:203–232, 1999.

[24] R. B. Northrop. *Introduction to Instrumentation and Measurements*. Taylor & Francis, 2nd edition, 2005.

[25] E. Pina, C. Prados, and A. Hernando. Large training effects in magnetic relaxation and anisotropic magnetoresistance in nanocrystalline exchange-biased Ni80Fe20/Co-o bilayers. *Phys. Rev. B*, 69:052402–4, 2004.

[26] W. P. Pratt, Q. Yang, L. L. Henry, P. Holody, W.-C. Chiang, P. A. Schroeder, and J. Bass. How predictable is the current perpendicular to plane magnetoresistance? *J. Appl. Phys.*, 79(8):5811–5815, 1996.

[27] PXI Systems Alliance. *PXI Hardware Specification*, 2nd edition, 2000.

[28] D. C. Ralph and M. D. Stiles. Spin transfer torques. *J. Magn. Magn. Mater.*, 320:1190–1216, 2008.

[29] C. Rennec, P. Niedermann, A. D. Kent, and Ø. Fischer. A vertical piezoelectric inertial slider. *Rev. Sci. Instr.*, 61:965–967, 1990.

[30] John G. Simmons. Generalized formula for the electric tunnel effect between similar electrodes separated by a thin insulating film. *Journal of Applied Physics*, 34(6):1793–1803, 1963.

[31] J. C. Slonczewski. Current-driven excitation of magnetic multilayers. *J. Magn. Magn. Mater.*, 159, 1996.

[32] J. Tersoff and D. R. Hamann. Theory and Application for the Scanning Tunneling Microscope. *Phys. Rev.*, 50(25):1998–2001, 1983.

[33] J. Tersoff and D. R. Hamann. Theory of the scanning tunneling microscope. *Phys. Rev. B*, 31(2):805–813, 1985.

[34] S. Urazhdin and A. Nicholas. Effect of polarized current on the magnetic state of an antiferromagnet. *Phys. Rev.*, 99(4):046602(4), 2007.

[35] Gabriel Vasilescu. *Electronic Noise and Interfering Signals. Principles and applications*. Springer-Verlag, 2005.

[36] Rainer Waser, editor. *Nanolectronics and Information Technology*. Wiley, 2 edition, 2005.

[37] Z. Wei, A. Sharma, A. S. Nunez, P. M. Haney, P. A. Duine, J. Bass, A. H. MacDonald, and M. Tsoi. Changing Exchange Bias in Spin Valves with an Electric Current. *Phys. Rev.*, 98, 2007.

[38] G. Wexler. Size effect and non-local boltzmann transport equation in orifice and disk geometry. *Proceedings of the Physical Society of London*, 89:927, 1966.

[39] Roland Wiesendanger. *Scanning Probe Microscopy and Spectroscopy: Methods and Applications*. Cambridge University Press, 1994.

[40] Haiwen Xi and Scott Franzen. Characterization and analysis of the training effect of exchange bias in coupled NiFe/IrMn bilayers. *J. Appl. Phys.*, 101:09E513–3, 2007.

[41] Haiwen Xi, Scott Franzen, Sining Mao, and Robert M. White. Exchange bias relaxation in reverse magnetic fields. *Phys. Rev. B*, 74:014434–5, 2007.

[42] Yuan Xu, Shuai Wang, and Ke Xia. Spin-Transfer Torques in Antiferromagnetic Metals from First Principles. *Phys. Rev.*, 100(2):226602(4), 2008.